IEEE Transactions on Robotics (T-RO) paper, presented at ICRA 2026, Vienna, Austria. Cite as T-RO paper.

EeLsT: An Energy-efficient Long-short Term Approach for Sustainable Sailboat Autonomy in Disturbed Marine Environment

Qinbo Sun[1,2], Weimin Qi[1,2] and Huihuan Qian[1,2,†]

***Abstract*—Sailboats are purely wind-driven and thus have great potential for long-term voyaging. For robotic sailboats, the constraints on the energy of the control boards, sensors, communication modules, and actuators are crucial to the sustainability of automation. Reducing the control frequency of actuators is crucial for energy conservation. This study proposes an energy-efficient long-short term (EeLsT) approach for sustainable sailing. In EeLsT, long-term and short-term observers are designed to adaptively take control decisions for time-varying environmental influences (e.g., waves and currents). Our approach can be generally applied as an energy management module in sailing robots. It explicitly leverages the sailing motion characteristics and the dynamic model of the robot considering marine disturbances. We have designed an experimental enhanced simulation platform to evaluate motion performance and energy consumption. Both baseline approach and the scheme incorporating EeLsT method (refer to as EeLsT approach in the subsequent sections) have been conducted. In simulation, EeLsT approach saves 31.8% energy. In the real marine environment, experiments are conducted with OceanVoy, a catamaran sailing robot. The results show that 27.4% of the energy is saved during stable sailing. In long-term sailing, compared to the standby mode when the motors are not working, the average power of the full automation mode has increased by no more than $1\,\mathrm{W}$, i.e. 4% relatively.**

***Index Terms*—Sustainable autonomy, energy-efficient long-short term approach, environmental disturbances, sailing robots**

Fig. 1. (a-c) Sample images of OceanVoy sailing day and night in the marine environment. (d) 30-day reciprocated sailing route (left) and experimental field taken with a panoramic camera mounted on the robot mast (right).

I. Introduction

SUSTAINABLE autonomy of field robots in unstructured environments heavily depends on reliable energy supply. When using rechargeable batteries as an energy source, it is essential to ensure timely replenishment of power through measures such as recharging [1], [2], [3] or harvesting solar energy [4]. Furthermore, reducing energy consumption at the hardware [5] or algorithm level [6] is a common measure.

Robotic sailboats, as shown in Fig. 1, are a distinctive category of underactuated field robots that possess the capability to leverage wind energy to achieve durable survival. Nowadays, the energy-saving and eco-friendly characteristics of sailing robots are enabling them to become vital tools in marine applications (e.g., ocean mapping [7] and ocean observation [8]). However, for automatic control of sailing robots' electrical and mechanical equipment in long-duration missions, the on-board batteries with limited capacity are one of the critical constraints. Therein, reducing energy consumption by performing an effective management scheme is an economical and effective measure to alleviate the energy dilemma in the vast and ever-changing marine environment.

Currently, according to our summary in Section 6.3 of [9], the exploration of this particular aspect remains limited. To fill this gap, we focus on the energy management problem of sailing robots toward persistent and long-range missions. In real sea environment, disturbances (e.g., waves, currents and tides) are commonly present and varied. The sailing robots need to save energy while performing stable motions in

This work was supported in part by the NSFC under Grant 62473324, in part by the Guangdong Basic and Applied Basic Research Foundation, University Stability Support Program from Shenzhen Science and Technology Innovation Commission under Grant 2022A1515240063, in part by the Shenzhen Institute of Artificial Intelligence and Robotics for Society under Grant AC01202101105, and in part by the Longgang District Shenzhen's "Ten Action Plan" for Supporting Innovation Projects, China under Grant LGKCSDPT2024002.

[1]Shenzhen Institute of Artificial Intelligence and Robotics for Society, The Chinese University of Hong Kong, Shenzhen, China.

[2]School of Science and Engineering, The Chinese University of Hong Kong, Shenzhen, China.

† Corresponding author is Huihuan Qian, hhqian@cuhk.edu.cn

IEEE Transactions on Robotics (T-RO) paper, presented at ICRA 2026, Vienna, Austria. Cite as T-RO paper.

perturbations. Therefore, our objective is to efficiently reduce the energy consumption of the entire system in a disturbed marine environment.

There have been some preliminary attempts for the energy management of sailing robots. Hertel *et al.* [10] used sensor data collected by a small sailboat on a lake to obtain the optimal parameters for control. An analysis for the impact of the sail and rudder activities on energy consumption was conducted. Plumet *et al.* [11] proposed to save energy by turning on the proportional-derivative controller only when the heading error was greater than an empirically set value. Experiments have been conducted on a lake. Sauze *et al.* [12] used an artificial neuro-endocrine controller to realize energy autonomy by modifying sailing behavior in a sensible manner and was validated in a lake. However, it is a preliminary exploration of basic feasibility and needs to sacrifice the sailing accuracy. Overall, there are almost no released quantitative results. An effective energy management approach has not yet been developed, and validation has not been carried out in a real marine environment.

In our recent research, we investigated the energy optimization with a hybrid control scheme in trajectory generation missions [13], in which pseudo-spectral optimal control and extreme seeking control for sailboat's rudder and sail, respectively. We have also proposed an energy-saving approach for the control frequency adjustment of actuators in path tracking [14]. Experiments were conducted in the lake and inner bay in [13] and [14], respectively, thus ignoring environmental disturbances. However, during long-term autonomy missions on the sea, the sustainability and stability of sailing are crucial, while environmental influences should not be overlooked. Furthermore, we are not primarily concerned with the accuracy of trajectory generation or tracking.

According to above-mentioned consideration, the main challenges include:

(1) An effective energy management approach for sailing robots to deal with the long-term autonomy considering environmental disturbances is still not available.
(2) Validation of the energy management method in the real marine environment is still rare.

Correspondingly, our contributions are two-fold:

(1) *A Novel Energy Management Approach:* Proposing EeLsT, an original and groundbreaking energy-efficient long-short term (EeLsT) approach to reduce the energy consumption of a robotic sailboat in long-term sailing. In EeLsT, sailboat's unique wind-driven motion and marine environmental disturbances were both taken into consideration. As shown in Fig. 1, the robotic sailboat, environment conditions and reciprocated sailing paths can be visually observed. Moreover, the robot's stable sailing performance was also ensured while reducing energy consumption.
(2) *Extensive Validation:* In addition to verifying the capabilities of sustainable sailing with the EeLsT approach in simulation, comprehensive validation was also performed in real marine environments. In simulation, control inputs (e.g., rudder commands) and environmental disturbances (e.g., waves, currents and tides) are treated as variables and compared by controlling only one variable at a time during each test. Similarly, experiments involve conducting comparative tests and analysis. Moreover, with the proposed EeLsT method, a long-term sailing lasting over $1200\,\mathrm{km}$ within 30 days was accomplished. In the long-term experiment, the maximum wind speed experienced was $13\,\mathrm{m/s}$, with sea states reaching a maximum level 3.

II. Related Works

This section gives a brief review of related work from the perspectives of existing energy management strategies, modeling schemes, and the way to deal with marine environmental disturbances.

A. Existing Energy Management Approaches

There have been abundant attempts at energy management of field robots that work in unstructured ground, air, and marine environments.

1) Approaches for Field Ground Robots: Energy consumption is an important consideration in motion/path planning of field ground robots. Wei and Isler [15] planned energy-efficient paths for ground robots by using energy costs as weights for edges of an environment graph. Wu *et al.* [16] generated energy-efficient coverage paths to explore a terrain surface, in which the energy consumption caused by gravity has been significantly reduced. Eiffert *et al.* [17] proposed a resource and response aware hierarchical path planning framework for agriculture robots. Gan *et al.* [18] learned an energy-aware reward map for legged robots using locomotion energy as the trajectory preference label.

There is also abundant literature revolving energy conservation strategies of ground robots. Adnane *et al.* [19] proposed a machine learning based energy management strategy for electric vehicles (EVs). A driving mode predictor was developed to minimize energy consumption in real time. A detailed review on energy management of EVs has been done in [20], [21]. They categorized the strategies into rule-based approaches and optimization-based methods. Efficiency, adaptability and computational complexity were the main criteria for the performance assessment.

2) Approaches for Unmanned Aerial Vehicles (UAVs): The necessity for the implementation of effective energy management strategies has arisen due to the restricted carrying capacity of lightweight batteries on UAVs. Onboard energy is usually treated as a constraint in mission/path planning of UAVs. Franco *et al.* [22] developed an energy model based on actual measurements. Then, it was used as a constraint for path planning of UAVs' area coverage missions. Bezzo *et al.* [23] used the control inputs to estimate the energy required for arriving goals. In precision agriculture, Tokekar *et al.* [24] proposed to save energy of a UAV by carrying it between deployment locations using an unmanned ground vehicle. Alyassi *et al.* [25] established an energy consumption model through extensive experimentation and analysis considering

IEEE Transactions on Robotics (T-RO) paper, presented at ICRA 2026, Vienna, Austria. Cite as T-RO paper.

wind, motion, weight and altitude. Manyam *et al.* [26] proposed hybrid path planning for a hybrid UAV by generating a path along with the energy mode switching control. Bi *et al.* [27] developed an energy-saving surfing algorithm for Nezha-mini by searching for the dynamic window conducive to takeoff in waves.

Moreover, there have been some reviews on the energy management of UAVs. They are categorized as rule-based strategies and fuzzy logic strategies in [28], [29]. Rule-based control is one of the most prevalent control methods.

3) Approaches for Unmanned Surface Vehicles (USVs): The energy consumption of marine robots is closely related to path planning. Lee *et al.* [30] proposed an energy-efficient path planner for USVs using a practical energy-based cost function. Kularatne *et al.* [31] proposed a graph search based method to plan energy and time optimal paths for USVs with designed cost functions. Niu *et al.* [32] proposed an energy-efficient path planning approach for USVs by integrating the Voronoi roadmap, Dijkstra's searching, genetic algorithm and coastline expanding. Zhang *et al.* [33] proposed to obtain an optimal path for the USV considering environmental effects and static obstacle avoidance. Li *et al.* [34] proposed a Genetic Algorithm based approach to minimize energy consumption.

There are also approaches aimed directly at energy management. Makhsoos *et al.* [35] proposed an energy management system to optimize the energy usage of a USV. Ma *et al.* [36] achieved energy consumption optimization by continuously analyzing the speed and path of the USV and predicting fuel consumption. Liang *et al.* [37] considered the necessity to control and coordinate the electric devices of a USV to exploit energy efficiently. Thompson *et al.* [38] stated an energy-aware mission planner for a USV, wherein energy consumption forecasts are utilized to mitigate the risk of an energy shortage.

Overall, unlike field ground robots, UAVs, and USVs equipped with stable propulsion systems, robotic sailboats rely completely on variable wind. For sailing robots, continuous maneuvering observation is necessary. Consequently, existing control methods cannot be directly applied.

B. Existing Sailboat Modeling Approaches

The modeling of sailboats is a complex problem and remains challenging today. Until now, commonly used sailboat models include 6-DoF (surge, sway, heave, roll, pitch and yaw) [39]–[41], 4-DoF (surge, sway, roll and yaw) [42]–[44] and 3-DoF (surge, sway and yaw) [45]–[47]. Accuracy and computational complexity are two aspects to consider when applying these models.

The 6-DoF models mostly appear in simulations, presenting all dynamics effects as accurately as possible. Avizzano *et al.* [39] developed a 6-DoF sailing simulator considering effects caused by wind, pilots and sea environment. Furrer [40] simulated a 6-DoF model for control of a catamaran. Buehler *et al.* [41] simulated the dynamic of the sailboat movement with a 6-DoF model. However, in real-world control systems, researchers tend to simplify the 6-DoF models to 3-DoF or 4-DoF models under the corresponding assumptions and approximations.

For models with 3-DoF, it is assumed that the sailboat is maintained on the water surface and only accounts for horizontal motions, excluding heave, pitch and roll. Elkaim *et al.* [48] simulated a 3-DoF nonlinear model for segmented trajectory following. Cruz *et al.* [49] obtained a 3-DoF model for auto-heading control of an autonomous sailboat. Jaulin *et al.* [46] proposed a 3-DoF model given by state space equations for battery charging task by transforming the sailboat into a windmill. Based on the model in [46], Melin *et al.* [45] verified the control and a state estimator of a sailboat named mini 12 in experiments. Saoud *et al.* [50] simplified a 6-DoF model to a 3-DoF one to generate a rudder controller and a sail trimming calculator. However, these works did not consider the rolling motion in their controller designs, while it actually plays an important role in the behavior of robots using the wind for propulsion. In rough sea conditions, exceeding the certain threshold for roll angle of a sailboat may even lead to the danger of capsizing.

By adding consideration for the roll motion, Xiao *et al.* [42] proposed a 4-DoF model for heading control of the sailing yacht. Fossen's vectorial stated space representation [51], [52] was used to derive the motion equations. To realize course control, modification on drag and restoration forces have been made in [43] comparing with that of in [42]. A 4-DoF mathematical dynamic model of a catamaran was simulated in [53], and an autopilot is designed based on it.

In this article, pitch and heave motion are neglected in the model, as these two factors have little impact on the navigation course. Furthermore, ignoring them is also for the purpose of reducing computational complexity.

C. Marine Environmental Disturbances

The flow field in the ocean has an important influence on the motion of robots [54]. Due to the low maneuverability of sailboats, the influence of environmental dynamics (e.g., waves and currents) cannot be ignored. Hereby, in the long time dimension, environmental factors (such as tides) can change the path significantly. Therefore, explicitly model the environment dynamics is necessary.

In Section II-A3, some energy management approaches of marine robots have considered environmental disturbances. In [30], the tidal current was simulated as the main environmental effects on path planning of USVs. Currents with different constant speed were applied in simulation. In [31], path planning of USVs with time-invariant ocean flow fields was verified in an indoor laboratory testbed. In [32], the current data was applied to USV's path generation. In [33], current and wind were assumed to remain constant within each hour.

In literature of Section II-B about sailboat modeling, only a very limited number of researches have considered environmental disturbances. In [41], buoyancy forces and approximated resistance of waves acting on an autonomous sailboat were included in simulation setting. Current and wave were modeled using Gauss-Markov processes in [48]

IEEE Transactions on Robotics (T-RO) paper, presented at ICRA 2026, Vienna, Austria. Cite as T-RO paper.

TABLE I
A COMPARISON BETWEEN THE MOST RECENT ENERGY MANAGEMENT STRATEGIES OF MARINE ROBOTS

	Approach	LL	HL	Model	Waves	Currents	Tides	Data	Expt.	Qnt.
Sailboats	Hertel *et al.* [10]	✓	✗	✗	✗	✗	✗	✓	✓	✗
	Plumet *et al.* [11]	✓	✗	✗	✗	✗	✗	✗	✓	✗
	Sauze *et al.* [12]	✓	✗	✗	✗	✗	✗	✓	✓	✗
	Sun *et al.* [13]	✗	✓	✓	✗	✗	✗	✗	✓	✓
	Sun *et al.* [14]	✓	✓	✗	✗	✗	✗	✓	✓	✓
	EeLsT	✔	✔	✔	✔	✔	✔	✔	✔	✔
USVs	Lee *et al.* [30]	✗	✓	✗	✗	✗	✓	✗	✗	✗
	Kularatne *et al.* [31]	✗	✓	✗	✗	✓	✗	✗	✓	✗
	Niu *et al.* [32]	✗	✓	✗	✗	✓	✓	✗	✗	✗
	Zhang *et al.* [33]	✗	✓	✓	✗	✓	✓	✗	✗	✗
	Li *et al.* [34]	✗	✓	✗	✗	✗	✗	✗	✓	✗
	Makhsoos *et al.* [35]	✗	✓	✗	✗	✗	✗	✗	✗	✗
	Ma *et al.* [36]	✗	✓	✗	✗	✗	✗	✗	✓	✗
	Liang *et al.* [37]	✗	✓	✗	✗	✗	✗	✗	✗	✗
	Thompson *et al.* [38]	✗	✓	✗	✗	✗	✗	✓	✓	✗

"LL" and "HL" refer to low-level control and high-level control, respectively. "Model" tells whether the dynamic model is introduced. "Waves", "Currents" and "Tides" are used to check whether these types of disturbances are considered. "Data" indicates whether historical data has been collected and utilized. "Expt." shows whether the real world experiments have been conducted. "Qnt." provides information on whether the quantitative results of energy savings have been provided.

and directly alter the velocity of the boat. However, waves and currents in the real ocean environment are difficult to directly estimate. Furthermore, the significant impact of tides on robotic sailboats in long-term sailing has not been considered. Therefore, more in-depth research should be conducted on sailboat modeling and experimentation with disturbance from waves, ocean currents and tides.

A detailed comparison of USVs and robotic sailboats is presented in Table I. Comparatively, our method will consider the listed factors in the most comprehensive manner.

This study is organized as follows: Section III gives the problem formulation. Section IV elaborates the motion of the sailing robot considering marine environment. Section V presents the EeLsT approach in detail. Section VI is about the simulation validation. Section VII shows the comparison experiments and long-term sailing experiment. Section VIII elaborates on the discussion and comparison. Section IX concludes the entire study and points out the potential future work. Section Appendix is about the dynamic model.

III. PROBLEM FORMULATION

The marine environment and the navigation of sailing robots pose significant complexity. Thus, this study adopts the following assumptions.

- Water is treated as an ideal fluid, possessing irrotational and incompressible properties.
- The primary disturbance in the marine environment is considered to be the plane currents, as stated in [55], therefore ignoring the pitch and heave motions.
- Experiments are conducted in an environment without exceptionally strong wind and water currents. The sea state does not exceed level 3 (with a wave height of 0.5-1.25 m), and the Beaufort number of the wind does not exceed level 6 (with wind speed of 10.8-13.8 m/s).

A. Problem Statement

Consider a robotic sailboat engaged in continuous reciprocated sailing across a given sea region, persisting until its energy is depleted or an unexpected situation causes an interruption. During reciprocating motion, both the voltage level of the battery and the surrounding environmental conditions are continuously observed to ensure that the robot sails safely with enough energy. In long-term sailing scenarios, as detailed in Section IV-A2, the challenge is to achieve stable navigation, minimizing energy consumption per unit of time based on the instantaneous wind field and environmental disturbances.

To fulfill the objectives of sustainable sailing, three fundamental components need to be addressed: analysis of sailing maneuvers (e.g., straight-line and turning segments), the modeling of a sailboat considering environmental disturbances, and the formulation of an effective energy management strategy. Table II presents the primary variables crucial for the subsequent content.

TABLE II
PARAMETERS DESCRIPTION

NOTATION	NOMENCLATURE
$\mathcal{P}$, $\mathcal{P}_i^{sl}$, $\mathcal{P}_j^{c}$	The sailing path, straight line parts and curve parts
i, j, t	The index of $\mathcal{P}_i^{sl}$/$\mathcal{P}_j^{c}$/time
M_{sl}, M_c	The maximum numbers of i and j
$\widetilde{Tw}$, $\widetilde{Aw}$	The toward/away wind sailing segments
$\widetilde{Ta}$, $\widetilde{Gy}$	The tacking/gybing parts during turns
θ_t, $\theta_{i,t}$, $\theta_{j,t}$	The course angle at time t of general/$\mathcal{P}_i^{sl}$/$\mathcal{P}_j^{c}$ path
θ^*, $\underline{\theta^*}$, $\overline{\theta^*}$	The predicted course angle and its lower/upper bound
ϵ_{sl}, ϵ_c	The selected thresholds for straight-line/curve
$\{F_E\}$, $\{F_B\}$	The earth-fixed/body-fixed frame
CoG, CoE	The center of gravity/effort
x, y, z	The translation of North/East/Down in $\{F_E\}$
ϕ, ξ, ψ	The Euler's angles of roll/pitch/yaw in $\{F_E\}$
ψ^*, $\underline{\psi^*}$, $\overline{\psi^*}$	The desired heading angle and its lower/upper bound
α_a	The attack of angle
δ_s, δ_r	The sail/rudder angle on $\{F_B\}$
u, v, w	The linear velocities for surge/sway/heave in $\{F_B\}$
$\boldsymbol{v}$	The linear velocity vector in $\{F_B\}$
p, q, r	The angular velocities for roll/pitch/yaw in $\{F_B\}$
Ψ_{tw}, a_{tw}	The true wind direction/speed
Ψ_{aw}, a_{aw}	The apparent wind direction/speed
$\boldsymbol{M}$, $\boldsymbol{M}_{RB}$, $\boldsymbol{M}_A$	The total/rigid/added mass matrix
$\boldsymbol{C}$, $\boldsymbol{D}$	The system Coriolis-centripetal/damping matrix
$\boldsymbol{\eta}$, $\boldsymbol{\eta}_w$	The robot/wave position and orientation vector in $\{F_E\}$
$\boldsymbol{\nu}$	The velocity vector in $\{F_B\}$
$\boldsymbol{\nu}_r$, $\boldsymbol{\nu}_c$	The resultant/current velocity vector in $\{F_B\}$
V_c, β_c	The current speed/angle
$\boldsymbol{g}$	The vector of restoration forces
$J(\boldsymbol{\eta})$	The coordinate transformation matrix between $\{F_E\}$ and $\{F_B\}$
$\mathbf{x}, \mathbf{u}, \mathbf{w}$	The vector of robot state, control and environmental effects
$\boldsymbol{\tau}$, $\boldsymbol{\tau}_{wave}$	The vector of propulsion/wave-induced forces
E	The total energy consumption
P_{avg}	The averaged power for the entire system
P_s	The requisite power for the system, except for the actuators
P_a	The power consumption related to the actuators
$\boldsymbol{\mathcal{D}}$, $\tilde{\boldsymbol{\mathcal{D}}}$	The collected/processed dataset
$\boldsymbol{\mathcal{D}}_{train}$, $\boldsymbol{\mathcal{D}}_{test}$	The training/testing dataset

B. Overview of Energy Management Scheme Design

For sustainable sailing, it is necessary to strike a balance between reducing energy consumption and sacrificing motion performance. *EA* and *MA* stand for energy analysis and motion analysis, respectively. Therefore, a balance needs to be achieved between *EA* and *MA*.

1) EA: It is divided into two distinct parts:

- The power required for the system to operate when the actuators are not working, represented as P_s. This includes the aggregate power consumption of the main

IEEE Transactions on Robotics (T-RO) paper, presented at ICRA 2026, Vienna, Austria. Cite as T-RO paper.

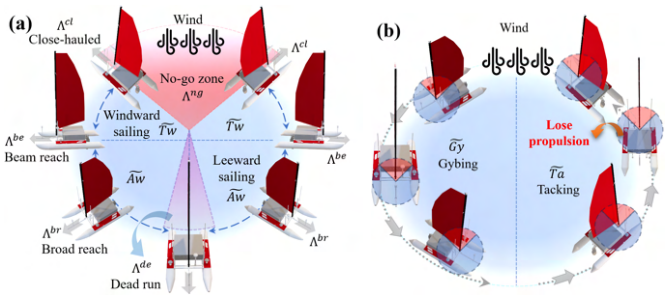

Fig. 2. Foundational aspects of the sailboat's motion with the wind blowing from the top. (a) Points of sail (PoS). (b) Two sailing maneuvers in turns.

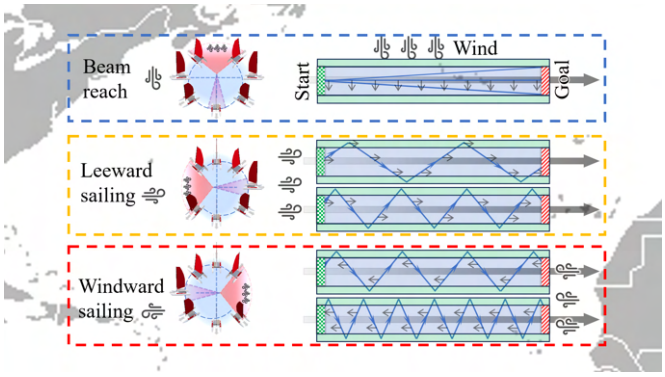

Fig. 3. Three typical long-term sailing scenarios: beam reach, leeward sailing and windward sailing. The "Start" and "Goal" sides are marked in green and red, respectively. Arrows on the blue path indicate wind direction.

board, control boards, sensors, localization and communication modules, etc.

- P_a contains the power consumption on the sail and rudder actuators. The actuator takes the form of a stepper motor arranged with a worm gear, and its load does not affect P_a.

In long-term sailing, the duration of a reciprocation is denoted by T, and the time period during which the actuator is in operation is T_a. The total energy consumption E is the sum of the integral of P_s and P_a:

$$E = \int P_s(t)dt + \int P_a(t_a)dt_a \tag{1}$$

where $t \in T$ and $t_a \in T_a$.

The average working power required by the whole system is calculated as

$$P_{avg} = E/T = P_s + P_a(T_a/T) \tag{2}$$

where P_{avg} ranges from the lower bound P_s to the upper bound $P_s + P_a$. P_{avg} can be used to demonstrate the performance of an energy management approach. Moreover, if P_{avg} is close to P_s, the superiority of the method can be validated.

2) MA: In this study, during reciprocated long-term sailing, the robot spends a lesser amount of time to executing turns in comparison to traversing straight lines. Therefore, we focus on *MA* of sailing in straight lines. Hereby, the mean and standard variance of motions are computed to assess the straightness.

3) Balance between EA and MA: It is imperative to appropriately allocate the total time between T_a and T to decrease energy consumption while ensuring optimal system functioning. If T_a is set to zero, it means that there is no control regulation, leading to potential errors in *MA* and compromising stability. Conversely, if T_a equals T, the sailing robot is consistently guided by the controller, enhancing precision and reliability in *MA*. Nevertheless, in this case, the energy consumption reaches its peak level.

IV. Foundations of Sailing Motion

Propelled by the wind, the movement of sailing robots exhibits complexity. This part delves into a comprehensive analysis of motion and modeling considering environmental disturbances.

A. Description of Sailing Maneuvers

1) Points of Sail: The motion encompasses various points of sail (PoS), a term denoting wind awareness that elucidates the course of a sailboat relative to the true wind direction over the water surface. As depicted in Fig. 2a, the primary points include:

* *No-go zone* Λ^{ng}: A sector within the red cone on either side of the true wind direction, where the sailboat is unable to sail due to a lack of propulsion.
* *Close-hauled* Λ^{cl}: A position as close to the wind as practically achievable, with the sail pulled taut.
* *Beam reach* Λ^{be}: At this point, the wind blows directly across the side of the sailboat, prompting a further easing of the sails.
* *Broad reach* Λ^{br}: It occurs when the wind comes from a quarter of the stern, and the sail is allowed to be loose.
* *Dead run* Λ^{de}: At this point, the wind flows over the stern, representing the most unstable PoS.

PoS facilitates the adjustment of sailing maneuvers, such as tacking and gybing, leading to enhanced speed and efficiency of the robot. Within Λ^{ng}, sailboats lose their propulsion, rendering them unable to avoid dangerous situations in emergencies. Moreover, the sailboat becomes unstable at Λ^{de}. Therefore, to ensure safety and optimize wind capture efficiency, it is necessary to maintain the sailboat within Λ^{cl}, Λ^{be} or Λ^{br}.

2) Objectives of Sustainable Sailing in A Given Region: The robotic sailboat continues to sail between the "Start" and "Goal" sides of the given blue region as shown in Fig. 3. The green areas on either side of the blue region are turning zones. As long as the robot maintains a sufficient energy availability and no unexpected situation arises, it will remain under control and sail along the blue sample motion.

According to different PoS, "Start" and "Goal" sides, three typical long-term sailing scenarios are beam reach, leeward sailing, and windward sailing. Thereafter, as shown in Fig. 3, the possible motions in blue for robotic sailboats are generated accordingly. For beam reach, the robot sails in nearly straight paths within Λ^{be}. In leeward sailing, the robot sails zigzagly and simultaneously avoids the unstable Λ^{de}. In windward sailing, the robot must avoid being trapped in

IEEE Transactions on Robotics (T-RO) paper, presented at ICRA 2026, Vienna, Austria. Cite as T-RO paper.

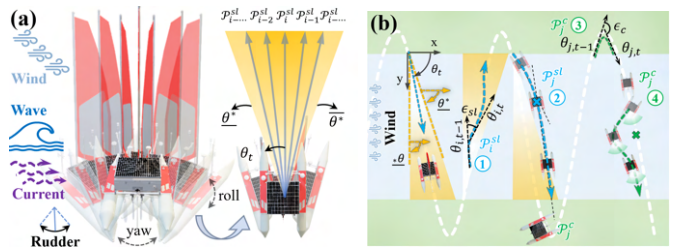

Fig. 4. Preliminaries for motion categories. (a) Influencing factors and motion responses. The yellow triangular area is formed by the lower and upper bounds of the predicted course angle, denoted as $\underline{\theta^*}$ and $\overline{\theta^*}$. (b) Example sailing scenarios in $\mathcal{P}_i^{sl}$ and $\mathcal{P}_j^c$. The blue area is the given target navigation area, and the green areas are for turning purposes. The white dotted line is the predicted sailing motions.

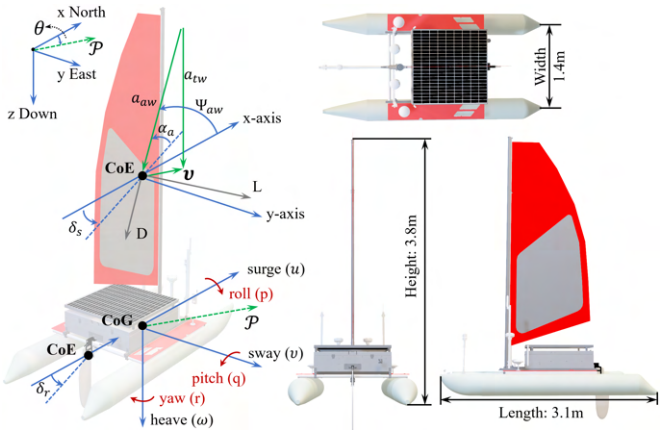

Fig. 5. The coordinate system and dimensions of the robotic sailboat.

Λ^{ng}. The sailing paths are also distributed zigzagly. Λ^{ng} is greater than Λ^{de}, so the motion of windward sailing typically involves more turns.

3) Motion Categories: The sailing path $\mathcal{P}_\iota^\varsigma$, with $\varsigma \in (sl, c)$ and $\iota \in (i, j)$, is partitioned into straight line parts $\mathcal{P}_i^{sl}$ and curve parts $\mathcal{P}_j^c$ as follows:

$$\begin{cases} \mathcal{P}_i^{sl} := \left\{ [\theta_{i,1}, ..., \theta_{i,t}]^T \in \mathbb{R}^t \middle| \, |\theta_{i,t} - \theta_{i,t-1}| \leq \epsilon_{sl} \right\} \\ \mathcal{P}_j^c := \left\{ [\theta_{j,1}, ..., \theta_{j,t}]^T \in \mathbb{R}^t \middle| \, |\theta_{j,t} - \theta_{j,t-1}| \geq \epsilon_c \right\} \end{cases} \tag{3}$$

where $i \in 1, 2, ..., M_{sl}$ and $j \in 1, 2, ..., M_c$. The thresholds ϵ_{sl} and ϵ_c of the course angle θ serve as criteria for judgment.

As depicted in the yellow triangular area in Fig. 4a, we expect the straight line path to remain within an acceptable range of course angles $(\underline{\theta^*}, \overline{\theta^*})$ while under the influence of wind, waves, currents and rudder adjustments. As shown in Fig. 4b, ① and ② show $\mathcal{P}_i^{sl}$ within and outside $(\underline{\theta^*}, \overline{\theta^*})$, respectively. In ②, the rudder guides the robot back to the straight line path. Meanwhile, there are two kind of curved paths $\mathcal{P}_j^c$: ③ the turning process, and ④ the straight line path curved by environmental disturbances, accidents or human intervention.

As shown in Fig. 2a, $\mathcal{P}_i^{sl}$ can be sub-divided into windward segments $\widetilde{Tw}$ and leeward segments $\widetilde{Aw}$,

$$\begin{cases} \widetilde{Tw} := \left\{ \mathcal{P}_i^{sl} \text{ toward the wind} \mid \text{between } \Lambda^{be} \text{ and } \Lambda^{cl} \right\} \\ \widetilde{Aw} := \left\{ \mathcal{P}_i^{sl} \text{ away the wind} \mid \text{between } \Lambda^{be} \text{ and } \Lambda^{de} \right\} \end{cases} \tag{4}$$

As illustrated in Fig. 2b, turning maneuvers in $\mathcal{P}_j^c$ can be distinguished into tacking $\widetilde{Ta}$ and gybing $\widetilde{Gy}$,

$$\begin{cases} \widetilde{Ta} := \left\{ \mathcal{P}_j^c \text{ into the wind} \mid \text{cross } \Lambda^{ng} \right\} \\ \widetilde{Gy} := \left\{ \mathcal{P}_j^c \text{ away the wind} \mid \text{cross } \Lambda^{de} \right\} \end{cases} \tag{5}$$

In sustainable sailing, both $\widetilde{Tw}$ and $\widetilde{Aw}$ are present in $\mathcal{P}_i^{sl}$ influenced by the wind field. Notably, for the turning process $\mathcal{P}_j^c$, $\widetilde{Gy}$ stands out due to its superior success rate and reliability compared to $\widetilde{Ta}$. As illustrated in Fig. 2b, while executing $\widetilde{Ta}$, the robot encounters Λ^{ng} resulting in loss of propulsion. On the contrary, during $\widetilde{Gy}$, the robot navigates without encountering it. Consequently, the robot will achieve consistent and reliable sailing through the utilization of $\widetilde{Gy}$.

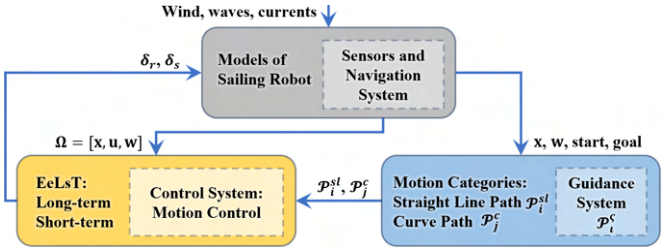

Fig. 6. The framework for Guidance, Navigation and Control (GNC) of sailing robots. The conventional framework is depicted in the dotted boxes, while our proposed framework is outlined within the three solid frames.

B. Environmental Disturbances Consideration

The sailing motion is determined by the collaborative interaction of inertia, gravity, and the aerodynamic and hydrodynamic forces acting on the robot. This part presents dynamic modeling, environmental influences, motion responses, and navigation strategies.

1) A Basic Model: The earth-fixed frame $\{F_E\}$ and body-fixed frame $\{F_B\}$ are introduced in Fig. 5. The assumption is made that the origin of $\{F_B\}$ aligns with the center of gravity (CoG) of the robot. Coordinates for forces acting on the foil are established at the sail's center of effort (CoE). In $\{F_E\}$, the position and attitude vectors of the robot are represented as $[x\ y\ z]^T$ and $[\phi\ \xi\ \psi]^T$, respectively. In $\{F_B\}$, the linear and angular velocity vectors are denoted as $[u\ v\ w]^T$ and $[p\ q\ r]^T$, respectively.

We neglect the pitch and heave motion, i.e. $w = q = 0$. Consequently, a simplified 4-DoF model for kinematics and dynamics of a sailboat is presented. The vector $\boldsymbol{\eta}$ represents position and attitude of the robot in $\{F_E\}$

$$\boldsymbol{\eta} = [x\ y\ \phi\ \psi]^T \in \mathbb{R}^2 \times \mathbb{S}^2 \tag{6}$$

and $\boldsymbol{\nu}$ is the velocity vector in $\{F_B\}$

$$\boldsymbol{\nu} = [u\ v\ p\ r]^T \in \mathbb{R}^4 \tag{7}$$

where $\mathbb{R}^n$ is an n-dimensional Euclidean space, and Euler angles are defined within the interval $\mathbb{S} = [0, 2\pi]$.

Based on the coordinate frames and parameter notations, the dynamics of a sailboat system can be derived as in [42]:

$$\begin{cases} \boldsymbol{M\dot{\nu}} + \boldsymbol{C}(\boldsymbol{\nu})\boldsymbol{\nu} + \boldsymbol{D}(\boldsymbol{\nu})\boldsymbol{\nu} + \boldsymbol{g}(\boldsymbol{\eta}) = \boldsymbol{\tau} \\ \dot{\boldsymbol{\eta}} = J(\boldsymbol{\eta})\boldsymbol{\nu} \end{cases} \tag{8}$$

IEEE Transactions on Robotics (T-RO) paper, presented at ICRA 2026, Vienna, Austria. Cite as T-RO paper.

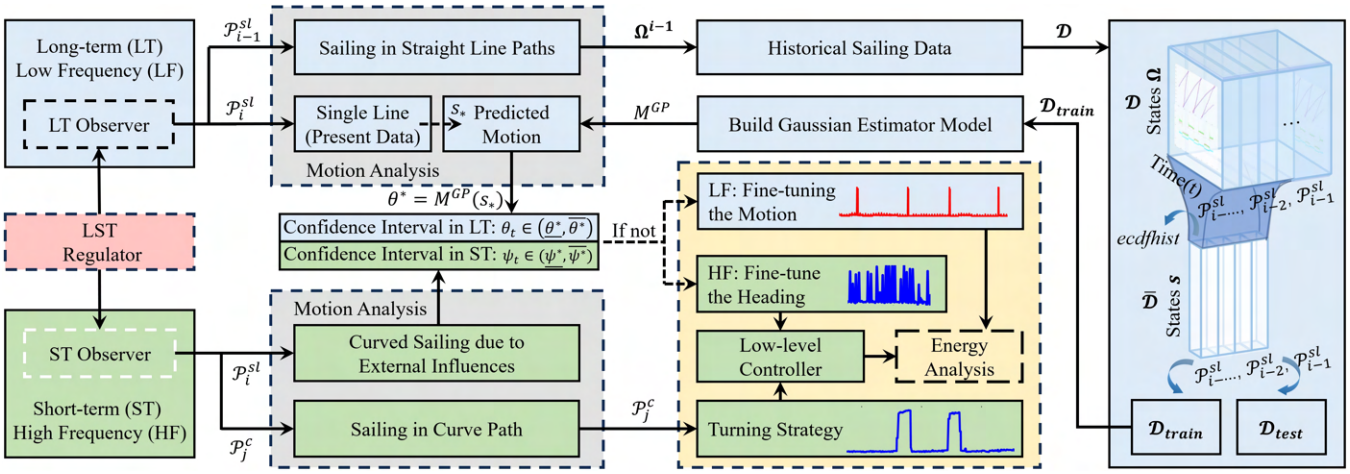

Fig. 7. Illustration of the EeLsT framework presented in this work. The long-term and short-term observers are shown in blue and green boxes respectively.

where the forces and moments, denoted by $\boldsymbol{\tau}$, are generated by actuators of the sail and rudder.

2) Effects of Environmental Disturbances: The impact of the marine environment on sailing robots can be analyzed from the perspectives of wind, waves and currents. The wind primarily acts on the sail foil, generating propulsive force for the robot's movement. The impact of wind disturbance on the hulls and masts is disregarded.

The effects resulting from waves and currents are significant disturbances that continuously affect the robot's motions. It is assumed that the wave effect adheres to the principle of superposition. Relative velocities are employed to substitute the forces that arise from currents. Further details about these calculations are provided in Appendix.

3) Motion Responses to Environmental Disturbances: *HF* and *LF* stand for high-frequency and low-frequency, respectively. Based on [56], disturbances caused by waves are designated as the *HF*, while currents are categorized as the *LF*. Correspondingly, the motion responses of marine environmental forces due to waves and currents can be conceptually classified into *HF* and *LF* types.

HF environmental disturbances primarily influence the robot's stability and safety. In the short-term period, it is crucial to observe the motion control response and prevent potential dangers. However, in the long-term period, the focus shifts to slow-varying sailing motions under *LF* environmental disturbances. Reasonable motion control strategies are beneficial for energy deduction.

4) GNC Scheme: The well-known Guidance, Navigation, and Control (GNC) system for robots [56] is shown in Fig. 6. We modify it to facilitate energy-efficient long-term sailing. Our GNC system incorporates classified sailing motion in guidance and the EeLsT module in control. As depicted in Section IV-A3, the path is divided into $\mathcal{P}_i^{sl}$ and $\mathcal{P}_j^c$ in the guidance system, and is used in the control system to make motion response decisions with the goal of reducing energy consumption.

V. EeLsT Approach

Using preliminary knowledge stated in Section III and Section IV, we elaborate our energy-efficient long-short term (EeLsT) approach in this section as shown in Fig. 7. *LT*, *ST* and *LST* stand for the long-term, short-term and long-short term, respectively. The scheme of EeLsT consists of long-term observer (*LTO*), short-term observer (*STO*), *LST* regulator (*LSTR*), *EA* and *MA*.

A. Long-term Observer (LTO)

LTO depicted in the blue boxes of Fig. 7 is employed to observe and maintain the sailing motions in $\mathcal{P}^{sl}$. *LF* current disturbances exert a notable impact on sailing motion, causing gradual sideways drift along the direction of the current over an extended period. To account for the disturbances, we will predict the robot course based on the collected historical sailing routes, and then use the predicted result as the desired course for control adjustments.

1) Data Collection: The state vector for $\mathcal{P}_i^{sl}$ in time series is Ω_t^i, including state vector $\mathbf{x}_t$, control inputs $\mathbf{u}_t$ and environmental effects $\mathbf{w}_t$ as follows:

$$\begin{aligned} \boldsymbol{\Omega}_t^i &\triangleq [\mathbf{x}_t\ \mathbf{u}_t\ \mathbf{w}_t]_i; \\ \mathbf{x}_t &\triangleq [\boldsymbol{\eta}\ \boldsymbol{\nu}\ \theta]_t; \\ \mathbf{u}_t &\triangleq [\delta_s\ \delta_r]_t; \\ \mathbf{w}_t &\triangleq [\Psi_{tw}\ a_{tw}\ \Psi_{aw}\ a_{aw}\ V_c\ \beta_c]_t \end{aligned} \tag{9}$$

where (Ψ_{tw}, a_{tw}), (Ψ_{aw}, a_{aw}) and (V_c, β_c) are speed and direction of true wind, apparent wind and current, respectively. As shown in the right part of Fig. 7, all data is stored in the collection $\boldsymbol{\mathcal{D}} = \{\Omega^i\}_{i=1}^{M_{sl}}$.

2) Data Processing: A distribution filter method is applied for data processing. The process involves utilizing the histogram based on the empirical cumulative distribution function (ecdfhist) to compute histogram bars. The results are provided in terms of heights and bin centers. The processed data $\bar{\boldsymbol{\mathcal{D}}} = ecdfhist(\boldsymbol{\mathcal{D}})$ are determined by the middle value of the bin centers, effectively eliminating the influences of high-frequency responses and other noise. Then, $\boldsymbol{\mathcal{D}}_{train}$ and $\boldsymbol{\mathcal{D}}_{test}$ are organized based on processed $\bar{\boldsymbol{\mathcal{D}}}$.

IEEE Transactions on Robotics (T-RO) paper, presented at ICRA 2026, Vienna, Austria. Cite as T-RO paper.

Algorithm 1 Long-term Observer: $LTO(\mathcal{P}_\iota^s, \mathbf{\Omega}_t^i, \theta^*)$

Input: $\mathcal{P}_\iota^s, \mathbf{\Omega}_t^i, \theta^*$
Output: $\mathbf{u}_t$
1: $\theta \leftarrow \mathbf{x}_t$; $\delta_r \leftarrow \mathbf{u}_t$; $\Psi_{tw}, V_c, \beta_c \leftarrow \mathbf{w}_t$
2: **if** $\mathcal{P}_{\iota,t-1}^s \rightarrow \mathcal{P}_{\iota,t}^s$ conform to $\mathcal{P}_{j,t-1}^c \rightarrow \mathcal{P}_{i,t}^{sl}$ **then**
3: $\quad \theta^* \leftarrow M^{\text{GP}} = \mathcal{N}(\mu_{s_*}, \Sigma_{s_*})$
4: $\quad \mathbf{u} \leftarrow \text{check}\theta(\theta, \theta^*)$
5: **else if** $\mathcal{P}_{\iota,t-1}^s \rightarrow \mathcal{P}_{\iota,t}^s$ conform to $\mathcal{P}_{i,t-1}^{sl} \rightarrow \mathcal{P}_{i,t-1}^{sl}$ **then**
6: $\quad \mathbf{u} \leftarrow \text{check}\theta(\theta, \theta^*)$
7: **end if**
8: **Function:** check$\theta(\theta, \theta^*)$
9: **if** θ in $(\underline{\theta^*}, \overline{\theta^*})$ **then**
10: $\quad$ **Return** $\mathbf{u}_t$
11: **else if** θ not in $(\underline{\theta^*}, \overline{\theta^*})$ **then**
12: $\quad \mathbf{u}_t \leftarrow \delta_r = sign(\theta - \theta^*)\Delta\delta_r + \delta_r$
13: $\quad LTO(\cdot)$
14: **end if**

3) Estimator Construction and Prediction: A Gaussian estimator model M^{GP} is constructed with $\boldsymbol{\mathcal{D}}_{train} = \{\mathbf{s}, \mathbf{y}\} = \{(s_n, y_n)|n = 1, ..., N\}$, where $s_n \triangleq [\theta\ \delta_r\ \Psi_{tw}\ V_c\ \beta_c]_n$ is the input and y_n is the output, and $N \in \mathbb{Z}_{>0}$. The output is the slow-varying course angle θ.

The latent function f is assumed to represent the correspondence between input and output. For the first-order system, a zero-mean Gaussian process [57] is applied to f as $y_n = f(s_n) + \epsilon_n$, $\epsilon_n \sim \mathcal{N}(0, \sigma_n^2)$. The prior on the target output is $\mathbf{y} \sim \mathcal{N}(0, \mathbf{K} + \sigma_n^2\mathbf{I})$. The covariance matrix $\mathbf{K}$ is calculated using the well-known squared exponential kernel function. Therefore, the mean and variance of the estimated paths can be calculated by

$$\begin{aligned} \mu_{s_*} &= \mathbf{k}_*^\top \left(\mathbf{K} + \sigma_n^2\mathbf{I}\right)^{-1} \mathbf{y} \\ \Sigma_{s_*} &= k(s_*, s_*) - \mathbf{k}_*^\top \left(\mathbf{K} + \sigma_n^2\mathbf{I}\right)^{-1} \mathbf{k}_* \end{aligned} \tag{10}$$

where $\mathbf{k}_*$ is the covariance matrix between the testing data s_* and s_n. The obtained M^{GP} model is utilized to guide *LTO* based on Algorithm 1.

4) Algorithm 1 for LTO Implementation: The input parameters of *LTO* contain the path $\mathcal{P}_\iota^s$, the state vector $\mathbf{\Omega}_t^i$ and the predicted course angle θ^*. The output parameter is the updated control command $\mathbf{u}_t$.

Line 1 retrieves the current course angle θ from $\mathbf{x}_t$, the rudder input δ_r from $\mathbf{u}_t$, and true wind direction Ψ_{tw}, current speed V_c and current angle β_c from $\mathbf{w}_t$. Line 2 checks whether the current path $\mathcal{P}_i^{sl}$ has switched from the curve path $\mathcal{P}_j^c$. When the condition in the line 2 is met, line 3 predicts the course angle θ^* with the well-trained Gaussian model M^{GP}. Line 4 checks the current and predicted course and executes adjustment control commands if necessary. Line 5 indicates that $\mathcal{P}_i^{sl}$ is still a straight-line path at the previous time-stamp. Then, line 6 is executed the same as line 4.

Lines 8 to 14 define the function check$\theta(\cdot)$. Lines 9 and 10 check whether θ is within $(\underline{\theta^*}, \overline{\theta^*})$. If the current θ is within the predicted results at a 95% confidence interval (e.g., ① in Fig. 4b), then the control input $\mathbf{u}_t$ remains constant. Otherwise (e.g., ② in Fig. 4b), $\mathbf{u}_t$ will be altered based on the course error and a small command for rudder adjustment $\Delta\delta_r$, as shown in line 12. The predicted course angle is considered the desired course angle when the heading deviation exceeds the threshold interval $(\underline{\theta^*}, \overline{\theta^*})$. It is then used to calculate the difference and update the controller. Hence, the fine-tuned motion will make the robot sail in an approximately straight line. Finally, in line 13, the new state will be passed into $LTO(\cdot)$ for processing.

Algorithm 2 Short-term Observer: $STO(\mathcal{P}_\iota^s, \mathbf{\Omega}_t^i, \theta^*)$

Input: $\mathcal{P}_\iota^s, \mathbf{\Omega}_t^i, \theta^*$
Output: $\mathbf{u}_t$
1: $\psi_t \leftarrow \mathbf{x}_t$; $\psi_d \leftarrow \theta^*$
2: $e = \psi_t - \psi_d$; $\delta_r \leftarrow \mathbf{u}_t$; $\Psi_{aw} \leftarrow \mathbf{w}_t$
3: **if** $\mathcal{P}_\iota^s$ is $\mathcal{P}_j^c$ **then**
4: $\quad \mathbf{u}_t \leftarrow \delta_r = sign(\Psi_{aw})\delta_r^{(max)}$
5: **else if** $\mathcal{P}_\iota^s$ is $\mathcal{P}_i^{sl}$ **and** ψ_t not in $(\underline{\psi^*}, \overline{\psi^*})$ **then**
6: $\quad \mathbf{u}_t \leftarrow \delta_r = k_p e + k_i \int e + k_d \dot{e}$
7: **end if**

B. Short-term Observer (STO)

As shown in green boxes of Fig. 7, *STO* instructs the robot to take control in a timely manner based on the observed situation. *HF* wave disturbances are the primary influences of *STO*. In disturbed marine environments, heading angle can timely reflect turning operations or abnormal situations. Therefore, *STO* will closely observe the heading angle and implement frequent and effective control responses.

1) Observation and Motion Response: *STO* observes the curve sailing segments $\mathcal{P}^c$: (1) turning procedures; (2) originally sailing in $\mathcal{P}^{sl}$, but curved by external influences. If the sailing robot deviates from the interval $(\underline{\psi^*}, \overline{\psi^*})$, the low-level controller will take effect and fine-tune the heading angle.

The motion response is carried out by a low-level PID (Proportional, Integral and Derivative) controller. It is commonly used in sailing robots with robust performance, thus it is denoted as the baseline (BL) method in this study.

2) Algorithm 2 for STO Implementation: Algorithm 2 performs the observation task in the same manner as Algorithm 1, with consistent input-output. However, it differs in its observation strategies and control laws. Specifically, line 1 obtains the current heading angle ψ_t from $\mathbf{x}_t$, and assigns θ^* to the desired heading angle ψ_d. In this case, ψ_d is set to track the target. Line 2 obtains the tracking error e, rudder δ_r and apparent wind direction Ψ_{aw}. Line 3 is used to check

Algorithm 3 *LST* Regulator: $LSTR(\mathcal{P}_\iota^s, \mathbf{\Omega}_t^i, \theta^*)$

Input: $\mathcal{P}_\iota^s, \mathbf{\Omega}_t^i, \theta^*$
Output: $LTO(\cdot), STO(\cdot)$
1: **while** energy available and safe **do**
2: $\quad \theta \leftarrow \mathbf{x}_t$
3: $\quad$ **if** $\mathcal{P}_\iota^s$ is $\mathcal{P}_i^{sl}$ **then**
4: $\quad\quad \varsigma \leftarrow sl$; $\mathcal{P}_\iota^s \leftarrow \mathcal{P}_i^{sl}$
5: $\quad\quad LTO(\cdot)$ and $STO(\cdot)$
6: $\quad$ **else if** $\mathcal{P}_\iota^s$ is $\mathcal{P}_j^c$ **then**
7: $\quad\quad \varsigma \leftarrow c$; $\mathcal{P}_\iota^s \leftarrow \mathcal{P}_j^c$
8: $\quad\quad STO(\cdot)$
9: $\quad$ **end if**
10: **end while**

IEEE Transactions on Robotics (T-RO) paper, presented at ICRA 2026, Vienna, Austria. Cite as T-RO paper.

whether the path is a turning maneuver. If the path is in $\mathcal{P}_j^c$, the control vector $\mathbf{u}_t$ will be updated by the maximum rudder to achieve the turn in line 4 (e.g., ③ in Fig. 4b). In line 5, if the path is in $\mathcal{P}_i^{sl}$ and the heading is not within the desired range $(\underline{\psi^*}, \overline{\psi^*})$ (e.g., ④ in Fig. 4b), the rudder will be updated according to the PID controller in line 6, where k_p, k_i and k_d are parameters for proportional, integral and derivative parts.

C. LST Regulator (LSTR)

In the red box of Fig. 7, the *LSTR* manages the utilization of *LTO* and *STO*. The selection of them is based on the category of the current path (i.e., $\mathcal{P}_i^{sl}$ or $\mathcal{P}_j^c$). Algorithm 3 provides the implementation details of the *LSTR*.

In Line 1, the *LST* regulator works normally under the condition that energy availability and safety requirements are satisfied, as clarified in problem statement in Section III-A. Line 2 retrieves the current course angle θ from $\mathbf{x}_t$. In line 3, if the current path $\mathcal{P}_\iota^\varsigma$ is from $\mathcal{P}_i^{sl}$, then the symbols ς and ι will be respectively represented as sl and i. In this case, $LTO(\cdot)$ and $STO(\cdot)$ should be recalled, as shown in lines 4 and 5. In line 6, if the current path $\mathcal{P}_\iota^\varsigma$ is from $\mathcal{P}_j^c$, then the symbols ς and ι are c and j, respectively. Finally, $STO(\cdot)$ should be recalled in line 8.

D. EA and MA

In Fig. 7, *EA* and *MA* are represented within yellow and gray dashed boxes, respectively. The confidence interval is used to balance fine-tuning the motions by *LTO* or performing low-level control by *STO*. If the working time (time for executing the control commands) of *STO* is longer than that of *LTO*, energy consumption will increase, and motion performance will be improved. Conversely, if *LTO* dominates, energy consumption will decrease, but motion performance in *LTO* will be worse. For sailing in disturbed marine environments, decreasing energy consumption while ensuring safety based on *EA* and *MA* contributes to the sustainability of the voyage. For further energy reduction, an extreme solution involves *STO* not influencing the low-level controller, and fine-tuning motion in *LTO* is not executed, i.e., $E = \int P_s(t)dt$.

VI. Simulation

In this section, we validate the effectiveness of EeLsT through simulated scenarios with different disturbances. A dataset will be generated to train and validate the M^{GP} model. Subsequently, quantitative results of the proposed EeLsT scheme and the BL method will be presented.

A. Simulate the Environmental Disturbances

To thoroughly analyze and evaluate the motion responses, we simulate three distinct scenarios:

s_1 : No wave disturbances;
s_2 : Simulated wave disturbances;
s_3 : Experimental enhanced wave disturbances.

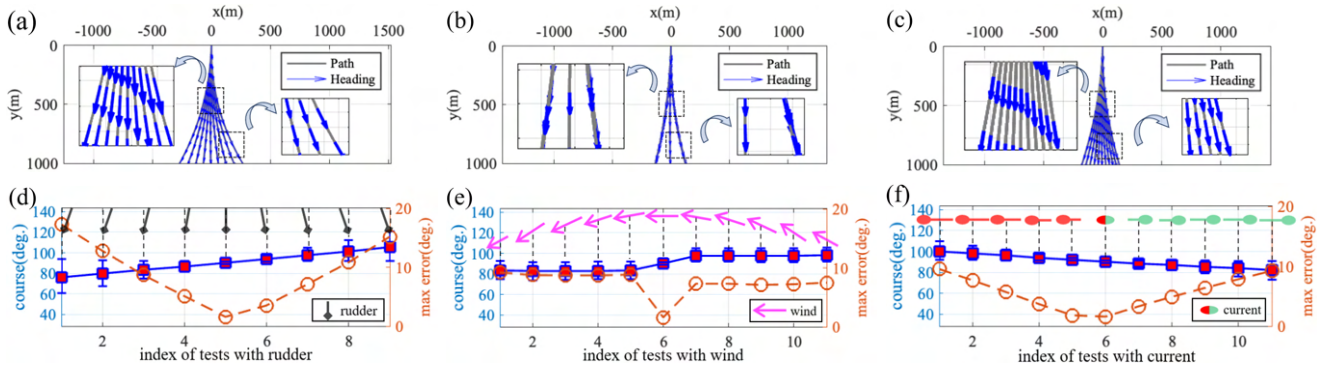

Fig. 8. Simulated s_1: $\mathcal{P}^{sl}$ without wave disturbances under different rudder angles (a, d), wind directions (b, e) and tidal currents (c, f). In (a-c), multiple $\mathcal{P}^{sl}$ are depicted using gray lines, accompanied by corresponding heading angles represented by blue arrows. (d-f) present error bars (y-axis on the left) for each course in (a-c) along with the respective maximum error (y-axis on the right).

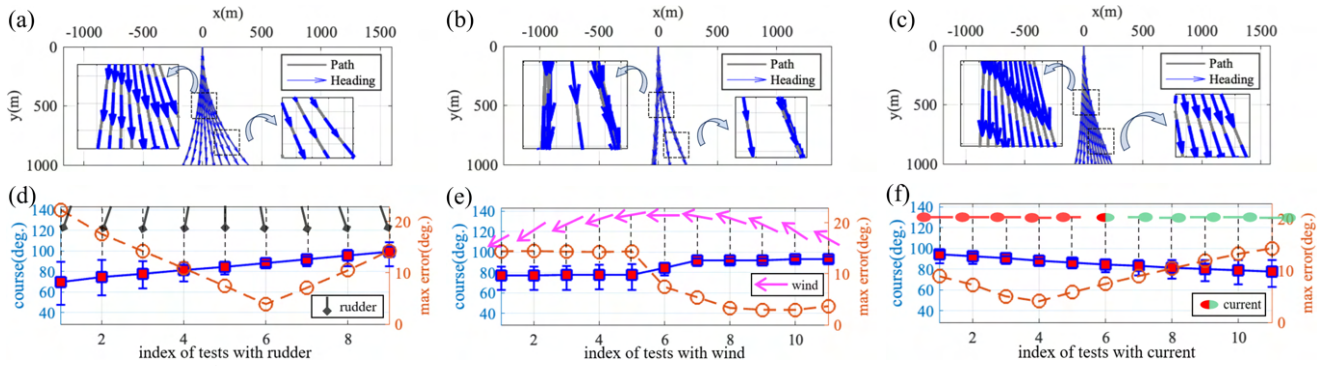

Fig. 9. Simulated s_2: $\mathcal{P}^{sl}$ incorporating modeled wave disturbances with different rudder angles (a, d), wind directions (b, e) and tidal currents (c, f).

IEEE Transactions on Robotics (T-RO) paper, presented at ICRA 2026, Vienna, Austria. Cite as T-RO paper.

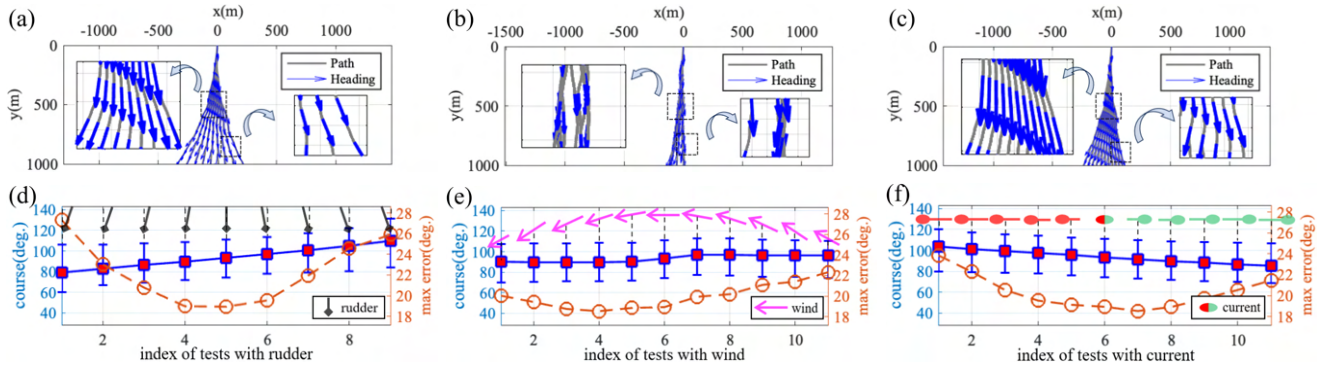

Fig. 10. Simulated s_3: $\mathcal{P}^{sl}$ subject to experimental enhanced waves with varying rudder angles (a, d), wind directions (b, e) and tidal currents (c, f).

1) Simulation for Three Scenarios: In s_1, there are three tests, and each test individually adjusts the rudder angles, wind directions, and tidal currents. Specifically, we first adjust the rudder with an interval $\Delta\delta_r$ (Figs. 8a, 8d), in which both wind directions and tidal currents remain constant. Secondly, the wind direction is altered within a predefined range using an interval $\Delta\Psi_{tw}$ (Figs. 8b, 8e). The rudder and currents remain constant throughout $\mathcal{P}^{sl}$. Thirdly, the current is modified while maintaining a constant rudder and wind, as depicted (Figs. 8c, 8f). Currents are induced by applying a horizontal force on the x-axis, varying from the negative to positive direction with an interval ΔV_c.

In s_2, we simulate wave disturbances based on Equation (12). For each $\mathcal{P}^{sl}$ presented in Fig. 9, adjustments have also been made separately to the rudder angles (Figs. 9a, 9d), wind directions (Figs. 9b, 9e) and tidal currents (Figs. 9c, 9f).

Despite selecting an appropriate wave model to generate disturbances, a notable gap persists between simulation and real-world scenarios. In s_3, to enhance the authenticity of simulated wave disturbances, we have chosen to gather wave motions from experiments in marine environment. Consequently, the experimentally enhanced data are utilized to simulate motion responses. Similarly to s_1 and s_2, adjustments are made separately to the rudder angles (Figs. 10a, 10d), wind directions (Figs. 10b, 10e) and tidal currents (Figs. 10c, 10f).

Given that our sail is soft and connected via a rope, its maximum deflection angle is mechanically constrained by the length of the rope. In all scenarios, with the same maximum sail angle, the sail passively shifts to the wind-aligned side according to the current angle of attack.

2) Motion Responses: The results in Figs. 8, 9 and 10 indicate the motion responses to the rudder, wind and current. It can be inferred that s_1 produces the smoothest paths, while s_2 results in paths with smaller variations but a larger maximum course error compared to s_1. The overall tendency of the course in s_3 is consistent with that observed in s_1 and s_2. However, the magnified region in s_3 shows apparent fluctuations compared to s_1 and s_2. Furthermore, s_3 leads to paths with the highest maximum course error. This suggests that s_3 more accurately represents the real marine conditions. Consequently, s_3 scenario will be employed to generate training data in the simulation.

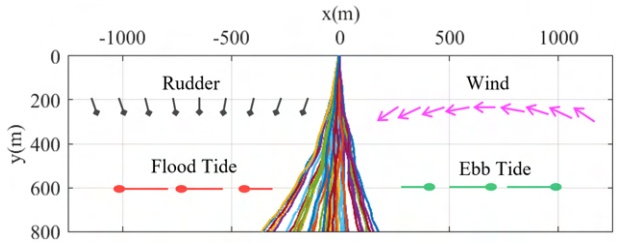

Fig. 11. Dataset obtained from s_3, where the colored lines represent $\mathcal{P}_i^{sl}$.

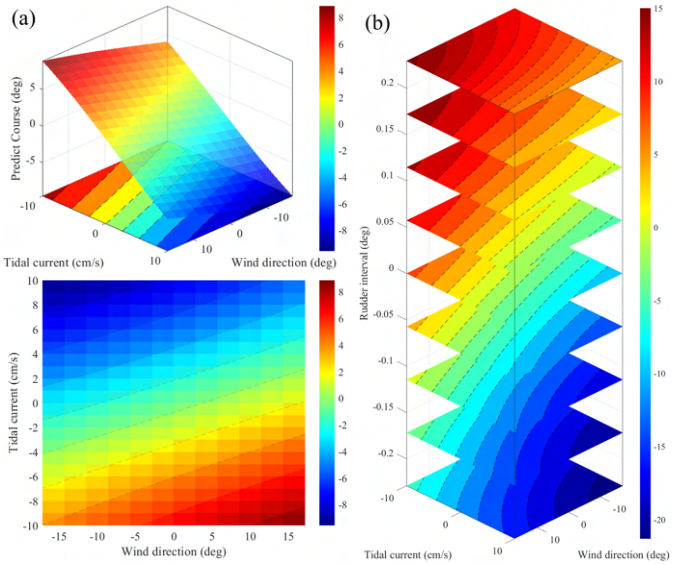

Fig. 12. Visualized estimator in simulation. (a) The prediction results in varying wind and tidal currents. (b) The influences of varying rudder in the z-axis. The color bar represents the predicted course angle.

B. Simulate the EeLsT Method

Given that s_3 is considered more realistic than s_1 and s_2, EeLsT method has been implemented, divided into data collection, data processing, prediction and validation.

1) Data Collection: As shown in Fig. 11, a simplified solution involves fixing the rudder in the initial state, maintaining a constant angle throughout each $\mathcal{P}^{sl}$. Consequently, the actuators of the sailing robot do not consume energy.

IEEE Transactions on Robotics (T-RO) paper, presented at ICRA 2026, Vienna, Austria. Cite as T-RO paper.

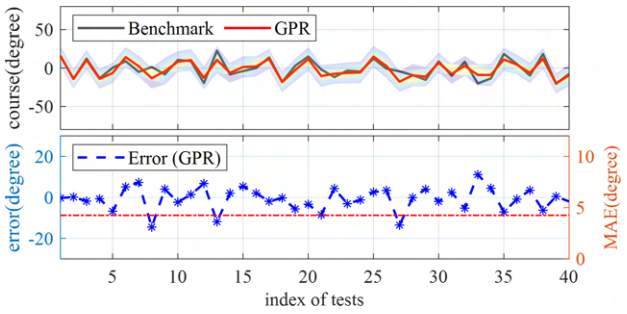

Fig. 13. Estimator validation on testing dataset. (Upper) The prediction results with 95% confidence interval versus benchmark. (Bottom) Errors (y-axis in blue) and MAE (y-axis in red) based on the M^{GP} model.

We simulate motion responses under varying initial rudder angles among $[-0.2°, 0.2°]$, wind directions in $[-30°, 30°]$ and current velocities in $[-20\,\text{cm/s}, 20\,\text{cm/s}]$. The intervals for $\Delta\delta_r$, $\Delta\Psi_{tw}$, and ΔV_c are denoted as $0.05°$, $6°$ and $4\,\text{cm/s}$, respectively. The data collected in $\mathcal{P}^{sl}$ is grouped into $\boldsymbol{\mathcal{D}}$.

2) Data Processing: The motion responses include oscillatory motions due to enhanced wave disturbances, requiring processing before constructing the dataset. The raw data $\boldsymbol{\mathcal{D}}$ are processed using the distribution filter, as mentioned in Section V-A2. The processed data are given by $\bar{\boldsymbol{\mathcal{D}}}$. Then, the training dataset $\boldsymbol{\mathcal{D}}_{train}$ and $\boldsymbol{\mathcal{D}}_{test}$ are organized. The numbers of path segments $\mathcal{P}^{sl}$ in both training and testing are 40.

3) Prediction and Validation: M^{GP} is applied to identify regression parameters and estimate the system model. The trained model is visually represented in Fig. 12. In Fig. 12a, the predicted course angle in the color map changes with wind direction and tidal currents. In the color map, warm and cool tones illustrate the positive and negative predicted course angles, respectively. It is obvious that the positive course angle in the warm region is associated with positive wind direction and negative tidal current, whereas the negative predicted course is characterized by opposite conditions. In Fig. 12b, each slice illustrates the visualized M^{GP} associated with a specific rudder angle, as depicted on the z-axis. The positive rudder angle yields the warm outcomes, while the negative angle generates the opposite results.

The trained model is validated using $\boldsymbol{\mathcal{D}}_{test}$, and the results are presented in Fig. 13. The upper figure demonstrates that the results predicted by M^{GP} align with the benchmark, with the color bar indicating the 95% prediction interval. In the bottom figure, the mean absolute error (MAE) on the right y-axis is $4.24°$. The minimum error, maximum error, root mean square error (RMSE) and standard deviation (Std) are $-14.49°$, $11.11°$, $5.57°$ and $10.33°$, respectively.

C. Evaluate the EeLsT Method

We conducted simulated tests using the BL method for comparison to evaluate the EeLsT method and demonstrate its effectiveness in terms of *EA* and *MA*. Firstly, tests with the BL method in s_1-s_3 are performed and labeled as (s_1-s_3)-BL. These tests aim to illustrate the impact of different wave

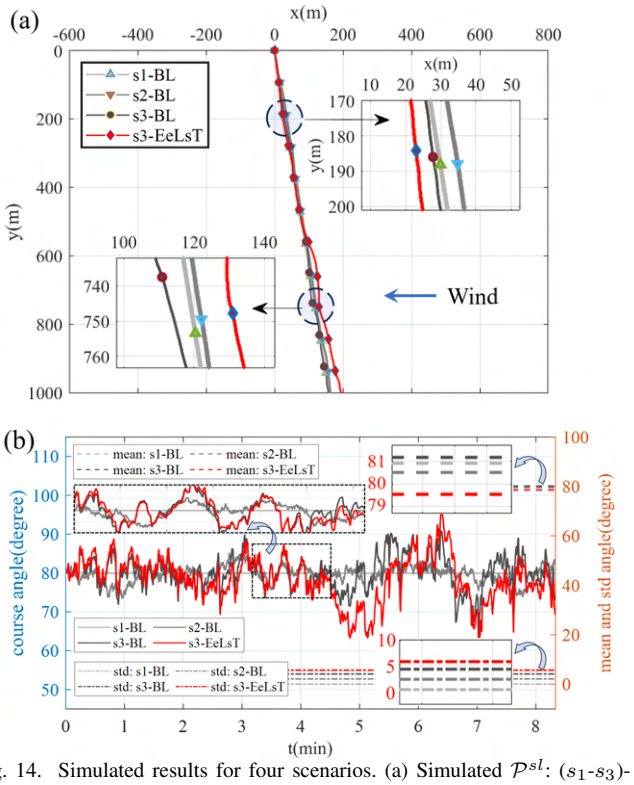

Fig. 14. Simulated results for four scenarios. (a) Simulated $\mathcal{P}^{sl}$: (s_1-s_3)-BL and s_3-EeLsT. The wind blows from the positive direction of x-axis in blue arrow. (b) The solid lines show the course angles. The dashed lines and dash dotted lines represent the mean and Std, respectively.

TABLE III
SIMULATION: *MA*, *EA* AND COMPARISON

Groups	Std (ψ)	Std (θ)	Error (MAE)	Energy (Total)	Power (Average)	Time (t)
s_1-BL	0.06°	0.08°	0.07°	3.62 (Wh)	24.54 (W)	531 (s)
s_2-BL	2.16°	2.27°	1.69°	5.10 (Wh)	34.38 (W)	534 (s)
s_3-BL	4.19°	4.30°	3.26°	5.41 (Wh)	35.92 (W)	542 (s)
s_3-EeLsT	5.71°	4.51°	5.84°	3.63 (Wh)	24.50 (W)	534 (s)

Std(ψ): Standard deviation of heading angle. Std(θ): Standard deviation of course angle. Error(MAE): Mean absolute error of heading angle and desired heading angle.

disturbances on motions and energy consumption. Next, we explore the EeLsT method in s_3 labeled as s_3-EeLsT.

1) (s_1-s_3)-BL: The simulations of (s_1-s_3)-BL are conducted under three distinct conditions: without waves, with modeled waves, and with enhanced waves. All tests begin from the same initial states and continue until reaching the desired states at a distance of 1000m along the y-axis.

2) s_3-EeLsT: In s_3-EeLsT, experimentally enhanced wave disturbances is added to create a realistic sea environment. The initial and desired states match those in (s_1-s_3)-BL. Therefore, the initial rudder action is fine-tuned to attain the desired states using the EeLsT method.

D. Performance Comparison for EA and MA

The resulting quantitative data of (s_1-s_3)-BL and s3-EeLsT are displayed in Figs. 14a, 14b and Table III. From the simulated paths shown in Fig. 14a, all four tests successfully

IEEE Transactions on Robotics (T-RO) paper, presented at ICRA 2026, Vienna, Austria. Cite as T-RO paper.

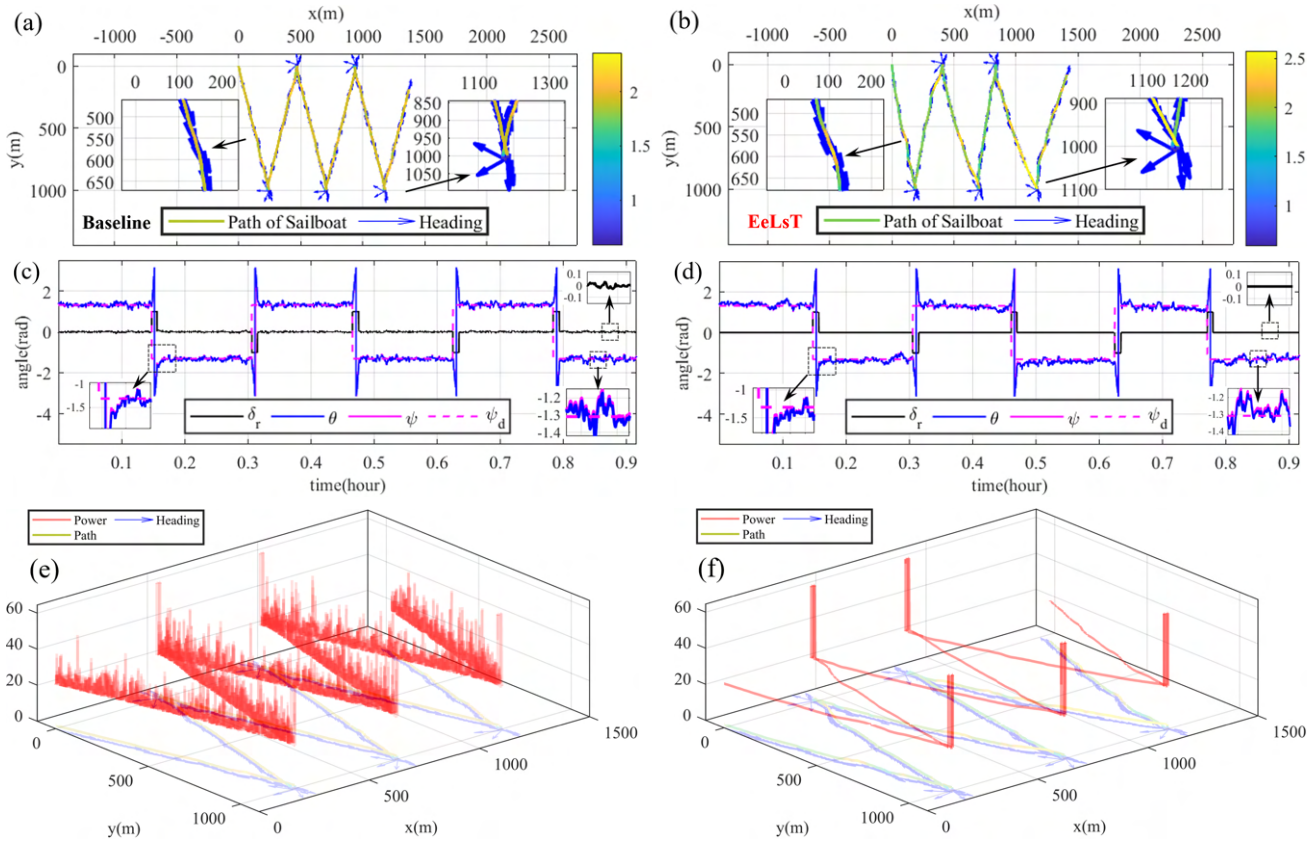

Fig. 15. Simulated *LT* scenarios. The wind blows from the positive direction of x-axis, with the heading indicated by a blue arrow and the speed represented by a color bar. (a) With BL method. (b) With EeLsT method. (c, d) The rudder, course, heading and desired angle are shown in black, blue, magenta and dashed magenta. (e, f) Red power maps in the z-axis direction (with unit watt) correspond to the transparent path.

reached the goal with similar courses. In Fig. 14b, the course with the lightest gray line, s_1-BL, remains constant. s_2-BL, represented by the lighter gray line, exhibits less variation and standard deviation (Std) than s_3-BL. The course with the darkest gray line is of s_3-BL. Meanwhile, the course of s_3-EeLsT is shown on the red line. Comparing the (s_1-s_3)-BL, it can be observed that s_3-BL has the largest variation and is consistent with real cases compared to (s_1-s_2)-BL. The *MA* of s_3-EeLsT is close to that of s_3-BL, indicating that the EeLsT method successfully achieves favorable motion performance even in the presence of environmental enhanced wave disturbances.

In Table III, Std(ψ), Std(θ) and error(MAE) show a reasonable increasing trend from s_1 to s_3. The unit of energy is W h, indicating the energy multiple of 1 A h@24 V. The average power consumption from s_1-BL to s_3-BL has increased. This trend can be attributed to significant wave disturbances and resulting variations in courses. When comparing s_3-EeLsT and s_3-BL, the former achieves a lower average power consumption, saving 11.42 W, indicating that the EeLsT method in s_3 is capable of saving energy while maintaining motion responses similar to those of BL in s_3. As mentioned in the validation, fine-tuning of the rudder in initial states enables energy conservation during the sailing process without consuming any energy on the actuator. It can be concluded that the EeLsT method results in an energy savings of 31.8% compared to the BL method.

E. Evaluation in Long-term (LT) Sailing Scenarios

We evaluate the performance of EeLsT method in *LT* sailing scenarios with multiple gybing maneuvers as shown in Fig. 15. In Figs. 15a and 15c, the path with BL method is straight with fewer deviations in heading ψ and course θ, resulting from the compensation of the controller. As a result, the rudder angle δ_r exhibits more fluctuations. In Figs. 15b

TABLE IV
SIMULATION: STD OF HEADING AND COURSE IN $\mathcal{P}^{sl}$ SEGMENTS

Items	Methods	$\mathcal{P}_1^{sl}$	$\mathcal{P}_2^{sl}$	$\mathcal{P}_3^{sl}$	$\mathcal{P}_4^{sl}$	$\mathcal{P}_5^{sl}$	$\mathcal{P}_6^{sl}$
Std(ψ)	BL	4.28	5.02	4.42	4.24	4.57	5.22
	EeLsT	5.82	6.58	6.65	5.41	7.04	7.45
Std(θ)	BL	4.27	5.08	4.41	4.23	4.57	5.22
	EeLsT	5.84	6.63	6.70	5.45	7.10	7.49
Error (MAE)	BL	3.40	3.72	3.46	3.30	3.53	4.21
	EeLsT	5.47	5.49	5.39	6.67	7.08	5.90
Power (Average)	BL	35.95	35.99	35.97	36.05	36.33	36.43
	EeLsT	24.50	24.50	24.50	24.50	24.50	24.50

The units for Std(ψ), Std(θ), Error(MAE) and Power(Avg) are °, °, ° and W.

IEEE Transactions on Robotics (T-RO) paper, presented at ICRA 2026, Vienna, Austria. Cite as T-RO paper.

TABLE V
SIMULATION: COMPARISON OF *MA* AND *EA* IN *LT* SCENARIOS

Methods	Distance (Total)	Std (ψ)	Std (θ)	Error (MAE)	Energy (Total)	Power (Average)
BL	6.15 (Km)	4.63°	4.63°	3.61°	35.53 (Wh)	38.76 (W)
EeLsT	6.28 (Km)	6.49°	6.53°	6.00°	25.43 (Wh)	27.74 (W)

and 15d, the sailing robot achieves a similar path using the EeLsT method, while the heading and course experience more fluctuations compared to the BL method. The EeLsT method adjusts the rudder angle δ_r to a suitable position after each gybing maneuver, thereby maintaining a constant δ_r during $\mathcal{P}^{sl}$. Consequently, comparing Figs. 15e and 15f, EeLsT method consumes less energy.

Two methods have the same total sailing time and control strategy in $\widetilde{Gy}$. For evaluation, *MA* and *EA* of six segments $\mathcal{P}^{sl}_{1,2,\ldots,6}$ are given in Table IV. Std(ψ), Std(θ) and error(MAE) of EeLsT scheme is slightly larger than that of BL method. During sustained maritime sailing, these metrics still met performance requirements under consideration of energy and safety. Notably, the power is significantly lower in EeLsT approach. Moreover, based on the red data in Table V, it can be concluded that the EeLsT method results in an energy savings of 28.4% when considering gybing maneuvers in long-term scenarios.

VII. EXPERIMENT

This section begins with an introduction to OceanVoy along with details about the testing fields in the challenging ocean environment and the control method for sails. Subsequently, OceanVoy is deployed to implement and evaluate the EeLsT method in environments, measuring quantitative energy consumption and motion responses. Finally, *LT* experiments are conducted, focusing on the endurance and sustained ability of the EeLsT method.

A. Robotic Sailboat: OceanVoy

As shown in Fig. 16, OceanVoy is retrofitted from a minicat310 sailboat with dimensions of $3.1\,\mathrm{m(L)} \times 1.4\,\mathrm{m(W)} \times 3.8\,\mathrm{m(H)}$ and a total weight of approximately $150\,\mathrm{kg}$. It is equipped with essential components, including control boards, sensors, communication components, a localization system, a $LiFePO_4$ type battery system with total capacity of $240\,\mathrm{A\,h@24\,V}$, and power modules. During experiments, the onboard voltage is remotely monitored by offshore experimenters via the power modules. If the voltage drops below a predefined threshold, a human-operated support vessel is deployed to provide assistance. For OceanVoy, the ranges of Λ^{ng} and Λ^{de} are 90° and 30°, respectively.

The Global Positioning System (GPS) records location, speed, and course angle. The weather station provides accurate wind speed and direction. The inertial measurement unit

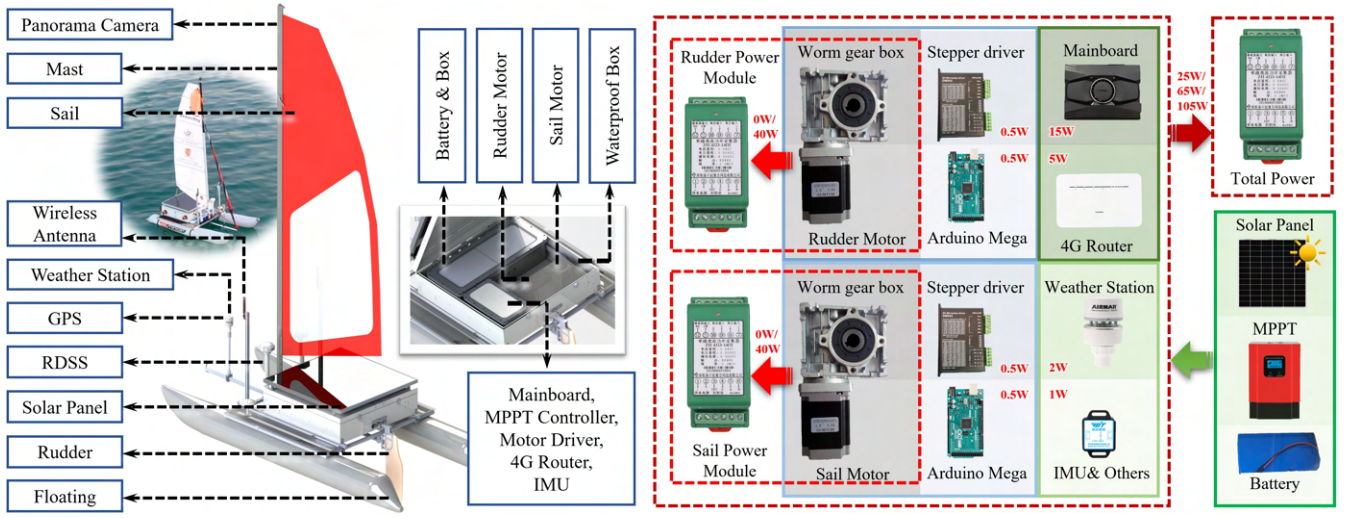

Fig. 16. The configuration of OceanVoy (left) and the onboard energy diagram (right), power distribution marked in red.

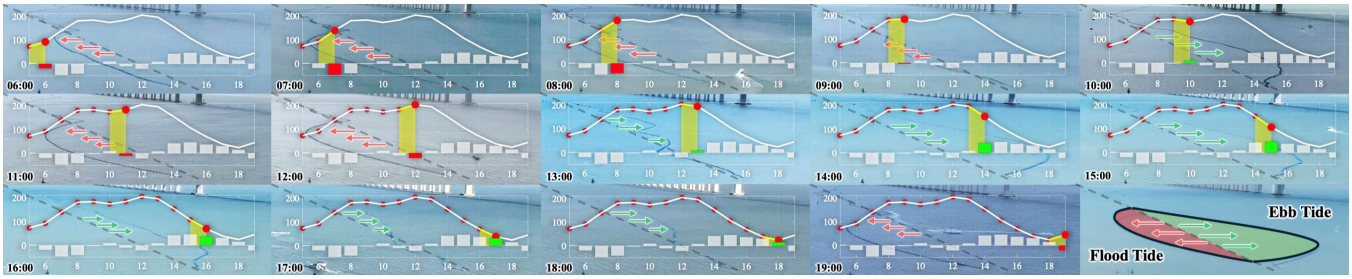

Fig. 17. The dynamic visual bar charts of floating rope movements throughout the day, illustrating tidal variations from sunrise (6:00 AM) to sunset (19:00 PM). The white curve depicts the tidal height, while the flood tide and ebb tide are distinguished in red and green arrows, respectively. The bar depicts the tidal range and corresponding the color of tidal current. The positive and negative tidal ranges correspond to the ebb and flood tide, respectively.

IEEE Transactions on Robotics (T-RO) paper, presented at ICRA 2026, Vienna, Austria. Cite as T-RO paper.

(IMU) captures roll, pitch, yaw, 3-axis acceleration, 3-axis angular rotation rate and 3-axis magnetometer data, crucial for recording the motions of the sailing robot. The sail motor and the rudder motor, responsible for controlling the sail and rudder, respectively, are stepper motors equipped with worm-gear boxes. This setup generates substantial torque for the payload while conserving energy through self-locking mechanisms, ensuring that there is no energy consumption when the control input remains unchanged.

The power consumption for each component is highlighted in red in Fig. 16. The green box represents the power supply system, and the red dashed box provides the power consumption of each module. The total power consumption is displayed in red dashed boxes. Specifically, for the rudder and sail actuators, the working power is 40 W, and the standby power with the self-lock mechanism is 0 W. The total power $P_s + P_a$ corresponds to three values depending on the operation conditions: 25 W (only system), 65 W (system + rudder/sail) and 105 W (system + rudder + sail).

For video data, a panorama camera is installed at the top of the sail mast. Several waterproof cameras are placed around the OceanVoy, used solely for data collection rather than surveillance or guidance. The cameras are powered by separate isolated power supplies, and their power consumption is not included in the operating power of the system. Additionally, offshore observation stations and photography drones are deployed to capture sailing videos.

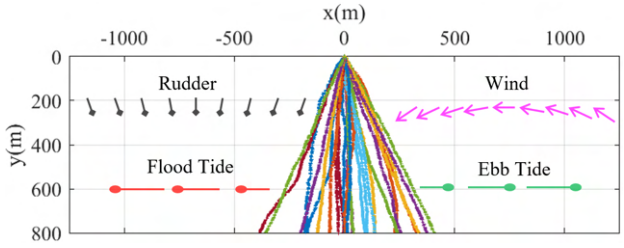

Fig. 18. The collected and rearranged dataset from experiments, showing variations in rudder, wind and tidal movement during $\mathcal{P}^{sl}$.

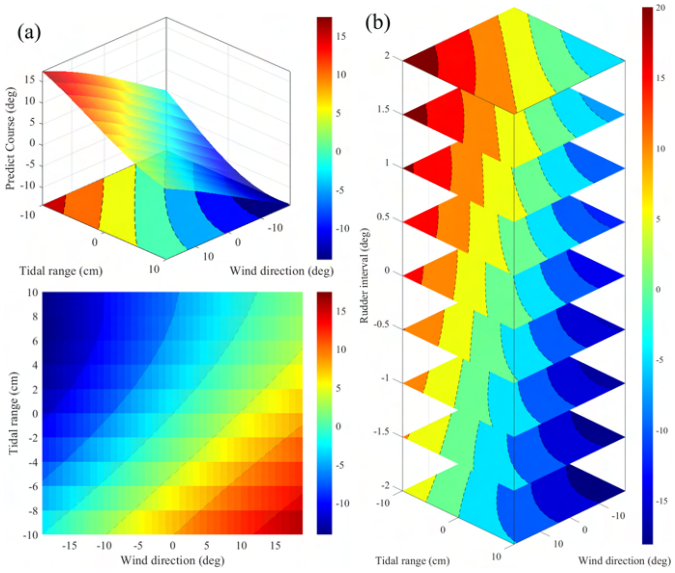

Fig. 19. Visualized estimated model in experiment. (a) The estimation results in different perspectives with varying wind direction and tidal range. The color bar represents the estimated course angle. (b) Considering the influences of varying rudder as shown in the z-axis.

B. Basic Settings

1) Disturbed Testing Fields: The experiments are conducted in the marine environment of Daya Bay in Shenzhen, China, characterized by its open water area and consistent monsoon winds. The primary disturbances in this region arise from oscillations and drifts caused by waves and currents.

The wave conditions are described using sea state. Additionally, the primary currents in the testing fields are tidal currents. Although accurate measurement of tidal currents is challenging, the tidal tables of testing site are provided by National Marine Data and Information Service (NMDIS) of China. The tidal range can be calculated according to the table. It effectively reflects changes in tidal currents, and can therefore serve as its representative. Consequently, the values of V_c are replaced with the tidal range. The unit of V_c aligns with the tide height, and its direction corresponds to β_c. As depicted in Fig. 17, 0° or 180° indicates ebb tide and flood tide, respectively. The pattern of floating ropes swaying with the current in the test field is consistent with the tidal information from NMDIS.

2) Sail Control Method: Sail control requires careful consideration of wind conditions, which is derived from two main reasons: (1) The power generated by the wind acting on the sails directly impacts the sailing speed. High speed is unfavorable for timely risk avoidance, while low speed makes it difficult to complete turning operations. (2) Improper sail angles can lead to capsizing or even overturning of the sailing robot. For example, failing to loosen the sail ropes when facing strong winds can cause the robot to capsize.

In this study, energy consumption and safety of robots are of greater concern compared to robot speed performance. Therefore, ensuring safe sailing and infrequent sail adjustment is crucial for energy-efficient sail control. As stated in simulation, the soft sail is connected via a rope and controlled by a stepper motor. The adjustment of the sail is performed using the tension induced in the sail–rope mechanism. With the maximum angle of the sail mechanically constrained by

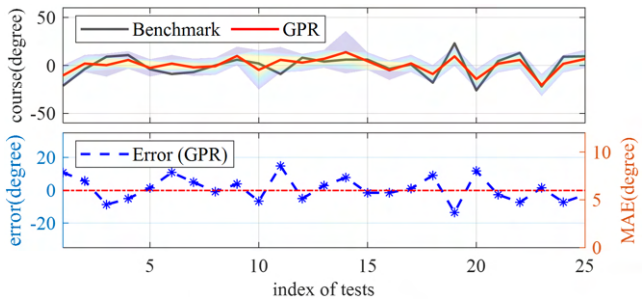

Fig. 20. Validation results and errors under actual sailing conditions. (Upper) The predicted results, confidence intervals, and benchmarks. (Bottom) The predicted errors in blue (y-axis in blue) dashed line and the MAE in red dashed line (y-axis in red).

IEEE Transactions on Robotics (T-RO) paper, presented at ICRA 2026, Vienna, Austria. Cite as T-RO paper.

rope length, the sail adaptively shifts to the wind-aligned side. We propose to passively change the angle of the sail according to the angle of attack. Specifically, the maximum sail angles 10°, 25°, and 35° are considered on different wind Beaufort scale 0-1, 2-5 and 6, respectively. Such correspondences are based on experience gained from extensive real-world experiments. Once the maximum sail angle and the length of the rope on the sail motor are determined, we can effectively avoid dangerous situations while saving energy.

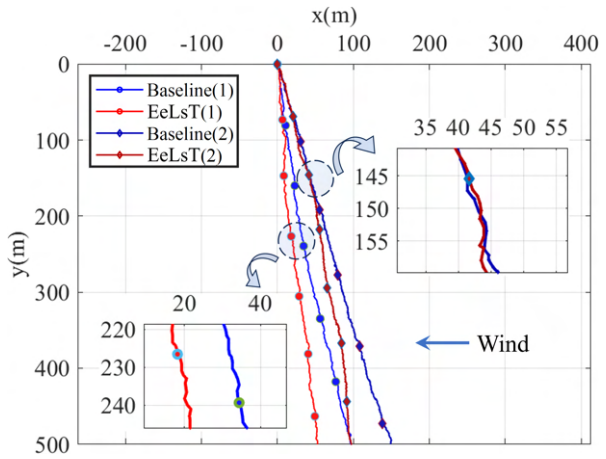

Fig. 21. Comparison of results from two groups of experiments employing BL and EeLsT methods. The blue arrow represents the wind direction.

C. Implement the EeLsT Method

We collect data through *LT* reciprocated sailing incorporating different rudder intervals $\Delta\delta_r$, wind fields and tidal ranges. Subsequently, we process the collected data to form the experimental dataset as shown in Fig. 18. The numbers of $\mathcal{P}^{sl}$ for both training and testing are 25. Notably, we process the tidal range by averaging it in each $\mathcal{P}^{sl}$, given the slow-varying nature of the data in each duration. The derived estimator model for *LTO* is presented in Fig. 19. Similarly in Fig. 12a of simulation, the visualization of the experimental model in Fig. 19a highlights a clear relationship among the predicted courses, wind direction and tidal range. The impact of varying rudder settings is depicted on the z-axis of Fig. 19b.

A series of tests involving $\mathcal{P}^{sl}$ are conducted to validate the accuracy of the M^{GP} estimator. As shown in Fig. 20, the estimated results are similar with that of the BL method. The MAE according to the right y-axis is $5.98°$. The minimum error, maximum error, RMSE and Std are $-13.55°$, $14.80°$, $7.22°$ and $7.69°$, respectively.

D. Evaluation in Real Sea Scenarios

Comparison experiments are devised to evaluate the motion performance and energy efficiency of the BL method and the EeLsT method. Different sets of $\mathcal{P}^{sl}$ are designated, denoted as group1 (BL(1), EeLsT(1)) and group2 (BL(2),

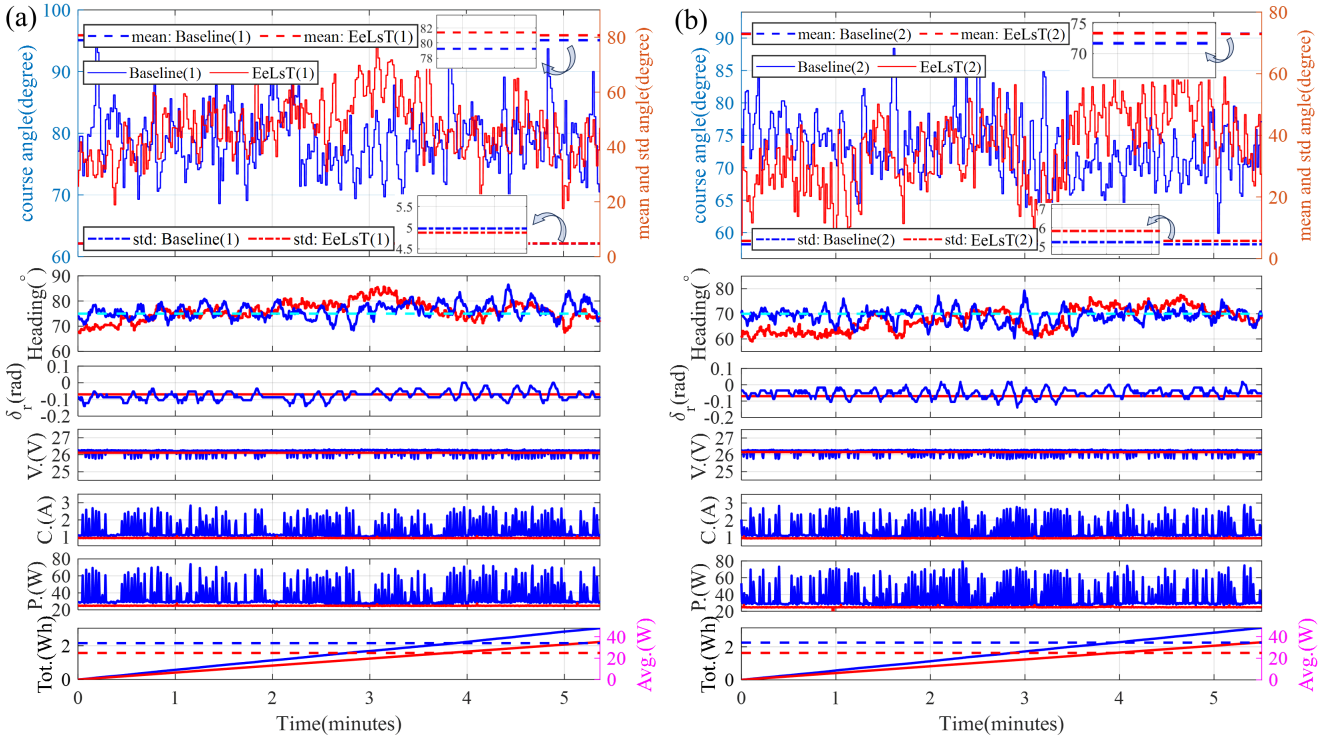

Fig. 22. *MA* and *EA* comparison for two groups of experiments in Fig. 21. *MA* elements on rows 1 to 3: in the 1st row, the solid lines represent the course angle (left y-axis), while dashed lines and dash-dotted lines represent the mean and Std angles (right y-axis), respectively. Blue and red represent the baseline (BL) and EeLsT methods, respectively, and this rule applies to all other subplots. The 2nd row exhibits the heading angles of two methods, and desired heading angle in cyan. The 3rd row is about the rudder angle of two methods. *EA* elements on rows 4 to 7 are voltage, current, power and energy consumption, respectively. In the 7th row, total energy is depicted with solid lines (left y-axis) while averaged energy is represented by dashed lines (right y-axis).

IEEE Transactions on Robotics (T-RO) paper, presented at ICRA 2026, Vienna, Austria. Cite as T-RO paper.

EeLsT(2)) as shown in Fig. 21. The experimental results are illustrated in Fig. 22a, Fig. 22b, and summarized in Table VI.

In Fig. 22, the performance with EeLsT method aligns with that of BL method. In bottom figures, the average energy consumption exhibits significant variations whereas course Std remains relatively smaller. A detailed examination of the data presented in Table VI indicates that the groups with BL method exhibit a smaller Std(ψ) and error(MAE) than EeLsT scheme. Nevertheless, there is no significant difference in the Std of the course.

Moreover, a comparison of average energy consumption reveals substantial energy-saving advantages with the EeLsT method. Compared to the BL method, group1 and group2 saved 26.9% and 27.8% of energy, respectively. Overall, the EeLsT method achieved an average energy savings of 27.4% compared to the BL method.

TABLE VI
EXPERIMENTS: *MA*, *EA* AND COMPARISON

Groups	Std (ψ)	Std (θ)	Error (MAE)	Energy (Total)	Power (Average)	Time (t)
BL(1)	2.82°	4.78°	2.46°	3.52 (Wh)	33.99 (W)	373 (s)
EeLsT(1)	2.93°	2.93°	4.78°	2.22 (Wh)	24.86 (W)	322 (s)
BL(2)	3.62°	4.63°	2.32°	3.15 (Wh)	34.36 (W)	330 (s)
EeLsT(2)	4.44°	4.06°	5.75°	2.32 (Wh)	24.82 (W)	337 (s)

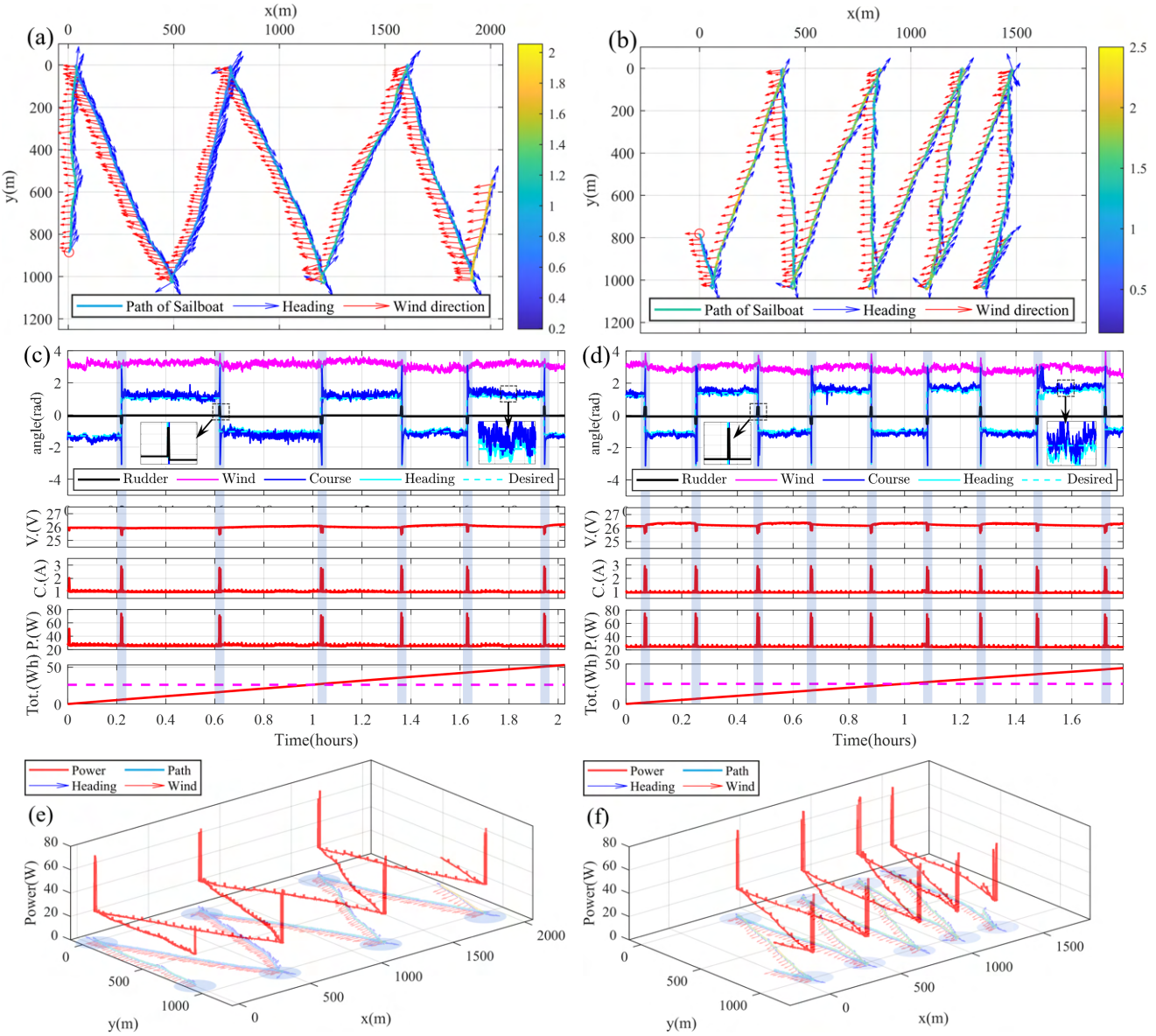

Fig. 23. Experimental results of two groups of *LT* sailing with EeLsT method. (a, b) The sailing path with color bar showing robot speed in m/s, blue arrows indicating heading, and red arrows representing the true wind direction. (c, d) The first row shows the angle variations over time, featuring the rudder angle in black, true wind angle in purple, course angle in blue, heading angle in cyan and desired heading angle in dashed cyan. The second to fifth rows present voltage, current, power and total energy consumption with respect to time. The dashed line indicates averaged energy consumption, and the gray bands represent turning parts in the path. (e, f) The power maps illustrating the entire power in watts. Each turn is marked with a blue circle.

IEEE Transactions on Robotics (T-RO) paper, presented at ICRA 2026, Vienna, Austria. Cite as T-RO paper.

TABLE VII
EXPERIMENTS: TWO CASES OF *LT* SAILING WITH EELST METHOD

LT Cases	Distance (Total)	Std (ψ)	Std (θ)	Error (MAE)	Energy (Total)	Power (Average)
Case1	7.83 (Km)	5.19°	7.07°	4.28°	53.07 (Wh)	26.18 (W)
Case2	10.02 (Km)	4.58°	6.02°	3.93°	44.93 (Wh)	25.19 (W)

TABLE VIII
DATA OF 30-DAY REAL-WORLD *LT* EXPERIMENTS

Days	Distance	Energy	Time	Power	Wind	Robot
1	16.52	0.26	10.24	25.73	2.22	0.41
2	24.01	0.43	16.37	26.10	2.46	0.41
3	28.04	0.44	17.46	25.42	2.24	0.39
4	17.58	0.23	8.80	25.90	2.93	0.50
5	13.63	0.17	6.49	26.86	3.63	0.50
6	36.85	0.63	24.00	26.40	3.28	0.42
7	65.43	0.61	24.00	25.23	4.24	0.66
8	56.92	0.62	24.00	25.96	3.53	0.59
9	32.72	0.52	19.24	26.80	2.33	0.41
10	18.74	0.17	6.62	25.33	3.20	0.72
11	70.10	0.60	24.00	25.13	2.91	0.67
12	49.79	0.62	24.00	26.03	2.09	0.51
13	70.48	0.62	24.00	25.65	3.54	0.68
14	114.03	0.62	24.00	25.72	4.91	1.23
15	56.77	0.62	24.00	25.67	2.01	0.56
16	84.42	0.62	24.00	25.96	3.80	0.89
17	50.86	0.47	18.35	25.36	2.59	0.69
18	20.80	0.22	8.59	25.65	2.78	0.59
19	50.01	0.62	24.00	25.97	2.38	0.51
20	48.61	0.61	24.00	25.45	2.13	0.49
21	43.83	0.61	24.00	25.58	1.97	0.45
22	41.08	0.48	18.79	25.47	3.86	0.51
23	32.72	0.36	13.75	26.28	3.44	0.58
24	44.06	0.62	24.00	25.99	1.89	0.46
25	13.80	0.28	10.68	25.94	1.46	0.33
26	15.52	0.12	4.41	26.24	3.72	0.86
27	31.92	0.28	10.85	25.71	2.78	0.73
28	15.79	0.19	7.32	25.73	1.84	0.52
29	43.34	0.63	24.00	26.16	1.86	0.47
30	17.90	0.26	9.68	26.40	1.95	0.47
AM	40.88	0.45	17.45	25.86	2.80	0.57
Total/ OA	Total 1226.27	Total 13.52	Total 523.64	OAP 25.82	OAW 2.81	OAR 0.59

The contents of each column are: Distance (Km), Energy (KWh), Time (Hour), Power (Watt), Wind Speed (m/s), Robot Speed (m/s), AM (arithmetic mean over 30 days), Total/OA (sum/overall-average over the entire *LT* voyage), OAP/W/R (overall average power, wind speed and robot speed), e.g., OAP= $\frac{13.52\ \text{KWh}}{523.64\ \text{h}} = 25.82$ W.

E. Long-term Sailing Experiments with EeLsT Approach

Two groups of selected *LT* sailing data with EeLsT method are presented in Fig. 23 under different wind conditions. Figs. 23a, 23c, 23e correspond to the first group, while Figs. 23b, 23d, 23f represent the second group. In Fig. 23a, OceanVoy sails at an average speed of $0.93\,\mathrm{m/s}$ in sea state 2, while the average wind speed is $4.11\,\mathrm{m/s}$. In Fig. 23b, OceanVoy operates at an average speed of $1.44\,\mathrm{m/s}$ with an average wind speed of $5.82\,\mathrm{m/s}$ in sea state 3. In Table VII, values of Std(ψ), Std(θ) and error(MAE) for two cases are close. The average power consumption in two cases is $26.18\,\mathrm{W}$ and $25.19\,\mathrm{W}$, respectively, accounting for variations in power.

With EeLsT, a *LT* voyage of more than 30 days is achieved in time-varying marine environment. The accumulated sailing data are shown in Table VIII, covering a cumulative distance of around $1226.27\,\mathrm{km}$. In Table VIII, all numerical values are reported in two decimal places to ensure clarity, consistency, and comparability. Accordingly, certain details should be clarified. For example, although the working power varies from Day 12 to Day 16, the recorded energy consumption remains the same across these days because of rounding to two decimal places. The overall average power P_{avg} (given in Equation (2)) over $1226.27\,\mathrm{km}$ is around $25.82\,\mathrm{W}$.

The graphical illustration for the data from Table VIII is given in Fig. 24a. It clearly illustrates the cumulative increase in sailing distance (blue line), energy consumption (red line) and time (orange line) during the *LT* voyage. In addition, the 30-day arithmetic means of power, wind speed, and robot speed are indicated by dotted lines.

Numerous experimental videos were collected, as depicted in Fig. 24b. These videos captured different perspectives of OceanVoy under varying marine and weather conditions. Furthermore, in the process diagrams of the two turns, it can be clearly seen from the enlarged images how the sail changes the windward side.

VIII. DISCUSSION

In this section, we discuss the results obtained from both simulation and experiments:

- Datasets Comparison: Both the simulated dataset (Fig. 11) and the experimental dataset (Fig. 18) originate from $\mathcal{P}^{sl}$, featuring diverse rudder, wind and tidal conditions. Despite disparities between simulated and real-world marine environments, the datasets demonstrate similar distributions.
- M^{GP} Model Comparison: M^{GP} models for simulation (Fig. 12) and experiment (Fig. 19) exhibit close correspondence in their color maps. The predicted course shows a positive correlation with rudder and wind, and an inverse relationship with tidal current.
- Validation Comparison: A review of simulations (Fig. 13) and experiments (Fig. 20) validated the efficacy of trained models with the test datasets. The MAE is marginally larger in the experiment, attributed to larger fluctuations in real marine disturbances.
- Path Comparison: $\mathcal{P}^{sl}$ in simulation (Fig. 14a) and experiment (Fig. 21) follow straight lines with varying fluctuations. EeLsT method shows effectiveness in experiments similar to the simulation.
- Quantitative Results: In Fig. 14b, Fig. 22, Table III and Table VI, EeLsT method exhibits comparable motion performance to the BL method, coupled with significantly lower energy consumption. Average energy savings are approximately 31.8% in simulation and 27.4% in experiment, respectively. Although the energy savings in the experiment are slightly smaller than in simulation, this discrepancy may be attributed to the faster controller response in simulation, which consumes less energy.
- *LT* Sailing Performance: Fig. 15 presents the *LT* sailing

IEEE Transactions on Robotics (T-RO) paper, presented at ICRA 2026, Vienna, Austria. Cite as T-RO paper.

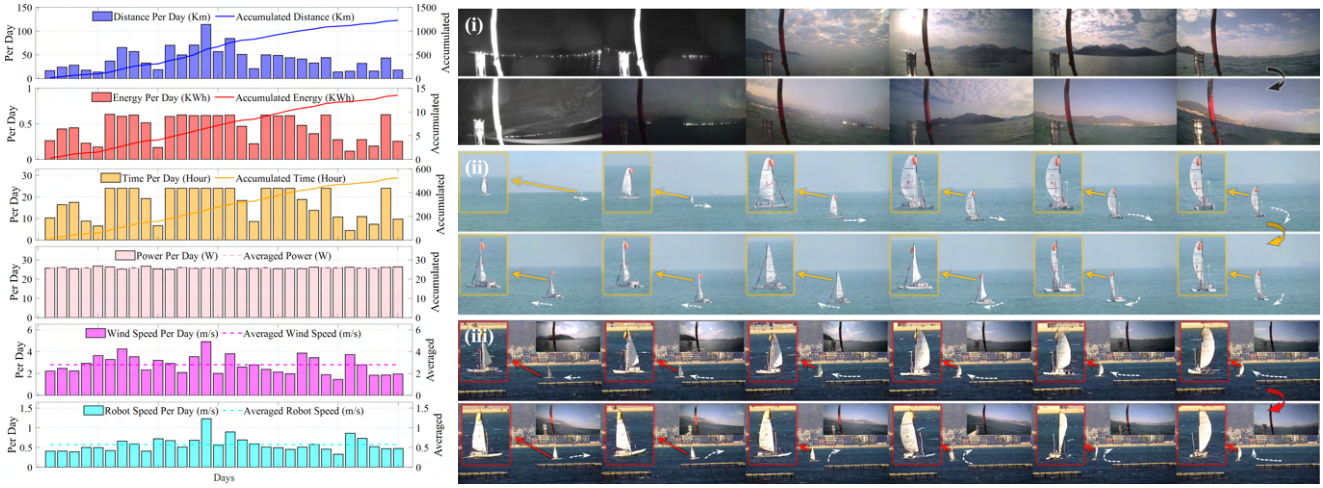

Fig. 24. Description of *LT* experiments. (a) Statistical comparison of the 30-day *LT* experiments. The left y-axis represents the daily data in bars, while the right y-axis displays the accumulated data in curves or averaged data in dotted lines. From top to bottom, the first three graphs illustrate the daily and 30-day accumulations of sailing distance, energy, and time, respectively. The following three graphs show the daily average and 30-day arithmetic mean power, wind speed, and robot speed, respectively. (b) Example snapshots of sailing over time. (i) Sailing during day and night. (ii) $\widetilde{Gy}$ in sea state 2. (iii) $\widetilde{Gy}$ in sea state 3 with whitecaps. In (ii) and (iii), the magnified views of OceanVoy are indicated by orange and red boxes, while the white dashed arrows depict the turning tendency.)

scenarios in simulation. Fig. 23 and Fig. 24a depict the *LT* experiments in the real marine environment. Based on the metrics calculated in Table IV, Table V, Table VII and Table VIII, the effectiveness and robustness of the proposed EeLsT method have been validated. In disturbed marine environments, achieving *LT* voyage requires the robotic sailboat to work with the overall average power P_{avg} close to the lower bound P_s in standby mode during sustained autonomy. Notably, as shown in Table VIII, the overall average power over $1226.27\,\mathrm{km}$ is around $25.82\,\mathrm{W}$. Considering that the system working power is theoretically around $25\,\mathrm{W}$ based on Fig. 16, our proposed method only added no more than $1\,\mathrm{W}$ (i.e. 4%) averaged power to the entire system during *LT* sailing over $1200\,\mathrm{km}$, which highlights the superiority of our proposed EeLsT approach to achieve energy-efficient and sustainable autonomy in disturbed marine environments.

IX. Conclusion

The proposed energy-efficient long-short term (EeLsT) approach is a novel energy management strategy tailored for sustainable sailing. Through the implementation of long-short term observers, we have extensively validated the EeLsT method in both simulation and real marine experiments.

It achieved significant energy savings while maintaining stable sailing performance. Compared to the BL method, approximately 31.8% and 27.4% of energy were saved in the simulation and experiment, respectively.

Leveraging the benefits of this approach, we successfully accomplished a cumulative sustainable voyage exceeding $1200\,\mathrm{km}$, operating with an overall average power of $25.82\,\mathrm{W}$. Remarkably, this method only adds an average power of $1\,\mathrm{W}$ to the entire system, emphasizing its significant advantages in real marine environments.

In the future, further research can be explored as follows: (1) This study shows the effectiveness of the EeLsT method in *LT* sailing, while the potential and generalization with other types of sailing robot (e.g., single-hulled and trimaran) is still an open question. Analyzing the relationships between these variations will enhance the versatility of the proposed method. (2) Valuable experience has been accumulated in the more than $1200\,\mathrm{km}$ sailing, challenges such as capsizing and breakdowns were encountered. The development of larger sailing robots capable of navigating beyond sea state 3 is a promising direction. This expansion allows for more extensive *LT* sailing, providing valuable insights into the method's performance under diverse conditions. OceanVoy460 [8], with a larger scale and payload is underway. (3) The wealth of collected sailing data, environmental information, and videos can be curated into a comprehensive dataset. It holds immense potential for embodiment learning or surveillance systems training, encompassing aspects such as robot monitoring, weather analysis, and abnormality monitoring.

Appendix

This part provides supplementary content for Section IV-B2, including considerations for environmental disturbances, as explained in [56].

Wave Effect: the wave-induced forces and moments are calculated as

$$\boldsymbol{\tau}_{\text{wave}} = \boldsymbol{\tau}_{\text{wavel}} + \boldsymbol{\tau}_{\text{wave2}} \tag{11}$$

where the first-order wave-induced force $\boldsymbol{\tau}_{\text{wave1}}$ refers to the zero-mean oscillatory motion, known as wave frequency motion. The second-order wave-induced force $\boldsymbol{\tau}_{\text{wave2}}$ is a slowly varying component, without zero mean.

IEEE Transactions on Robotics (T-RO) paper, presented at ICRA 2026, Vienna, Austria. Cite as T-RO paper.

In this article, we use JONSWAP wave spectra to model $\boldsymbol{\tau}_{\text{wave1}}$ with assumption of finite depth and limited fetch. d denotes the wave drift force $\boldsymbol{\tau}_{\text{wave2}}$ modeled as slowly varying bias terms (Wiener processes). Utilizing the superposition principle, the combination of first- and second-order wave-induced force can be determined as follows

$$\boldsymbol{\tau}_{\text{wave}} = h(s)w + d \tag{12}$$

where $h(s)$ is a simplified and effective approximation function representing the wave force. w is a Gaussian white noise process. Then, the waves forces and moments acting on the model is

$$\boldsymbol{M}\dot{\boldsymbol{\nu}} + \boldsymbol{C}(\boldsymbol{\nu})\boldsymbol{\nu} + \boldsymbol{D}(\boldsymbol{\nu})\boldsymbol{\nu} + \boldsymbol{g}(\boldsymbol{\eta}) = \boldsymbol{\tau} + \boldsymbol{\tau}_{\text{wave}} \tag{13}$$

To compare different waves, we also conducted the experimental enhanced wave disturbance. The updated motion of sailing robot can be linearly superpositioned by adding two motion components

$$\boldsymbol{\eta} = \boldsymbol{\eta} + \boldsymbol{\eta}_w \tag{14}$$

where $\boldsymbol{\eta}_w$ is the wave induced motion.

Current Effect: considering the hydrodynamic effect generated by currents, the model is adjusted as

$$\begin{aligned} &\boldsymbol{M}_{RB}\dot{\boldsymbol{\nu}} + \boldsymbol{C}_{RB}(\boldsymbol{\nu})\boldsymbol{\nu} + \boldsymbol{g}(\boldsymbol{\eta}) \\ &+\boldsymbol{M}_A\dot{\boldsymbol{\nu}}_r + \boldsymbol{C}_A(\boldsymbol{\nu}_r)\boldsymbol{\nu}_r + \boldsymbol{D}(\boldsymbol{\nu}_r)\boldsymbol{\nu}_r = \boldsymbol{\tau} + \boldsymbol{\tau}_{\text{wave}} \end{aligned} \tag{15}$$

where $M = M_{RB} + M_A$, $C(\boldsymbol{\nu}) = C_{RB}(\boldsymbol{\nu}) + C_A(\boldsymbol{\nu}_r)$, and the relative velocities $\boldsymbol{\nu}_r = \boldsymbol{\nu} - \boldsymbol{\nu}_c$. The calculation of the ocean current velocity vector $\boldsymbol{\nu}_c$ is based on the current speed V_c and angle β_c:

$$\boldsymbol{\nu}_c = \begin{bmatrix} V_c \cos(\beta_c - \psi) \\ V_c \sin(\beta_c - \psi) \\ 0 \end{bmatrix} \tag{16}$$

In ocean areas adjacent to coasts and fjords, *tidal currents* can reach high speeds, possibly exceeding $3m/s$. Therefore, when assessing the forces and moments imparted by the currents in long-term navigation, tidal currents should be considered as a major influencing factor.

The difference in height of the tidal currents can serve as an indicator of tidal currents. We make the assumption that the tidal currents are constant during each reciprocation. Therefore, the derivative of the current velocity with respect to time can be neglected (i.e. $\dot{\boldsymbol{\nu}}_c \approx \mathbf{0}$). Then the motion equation can be simplified to

$$\boldsymbol{M}\dot{\boldsymbol{\nu}} + \boldsymbol{C}(\boldsymbol{\nu}_r)\boldsymbol{\nu}_r + \boldsymbol{D}(\boldsymbol{\nu}_r)\boldsymbol{\nu}_r + \boldsymbol{g}(\boldsymbol{\eta}) = \boldsymbol{\tau} + \boldsymbol{\tau}_{\text{wave}} \tag{17}$$

where $\boldsymbol{C}(\boldsymbol{\nu}_r) = \boldsymbol{C}_{RB}(\boldsymbol{\nu}_r) + \boldsymbol{C}_A(\boldsymbol{\nu}_r)$.

REFERENCES

[1] E. Arribas, V. Cholvi, and V. Mancuso, "Optimizing uav resupply scheduling for heterogeneous and persistent aerial service," *IEEE Transactions on Robotics*, 2023.

[2] H. Fouad and G. Beltrame, "Energy autonomy for robot systems with constrained resources," *IEEE Transactions on Robotics*, vol. 38, no. 6, pp. 3675–3693, 2022.

[3] N. Mathew, S. L. Smith, and S. L. Waslander, "Multirobot rendezvous planning for recharging in persistent tasks," *IEEE Transactions on Robotics*, vol. 31, no. 1, pp. 128–142, 2015.

[4] P. A. Plonski, J. Vander Hook, and V. Isler, "Environment and solar map construction for solar-powered mobile systems," *IEEE Transactions on Robotics*, vol. 32, no. 1, pp. 70–82, 2016.

[5] M. Plooij, M. Wisse, and H. Vallery, "Reducing the energy consumption of robots using the bidirectional clutched parallel elastic actuator," *IEEE Transactions on Robotics*, vol. 32, no. 6, pp. 1512–1523, 2016.

[6] Y. Mei, Y.-H. Lu, Y. C. Hu, and C. G. Lee, "Energy-efficient motion planning for mobile robots," in *IEEE International Conference on Robotics and Automation, 2004. Proceedings. ICRA'04. 2004*, vol. 5. IEEE, 2004, pp. 4344–4349.

[7] M. Westington, N. Husain, H. Palmer, and N. Piszek, "2022 alaska coastal and ocean mapping summit report," 2023.

[8] W. Qi, Q. Sun, Y. Cao, and H. Qian, "Stable station keeping of autonomous sailing robots via the switched systems approach for ocean observation," in *2023 IEEE International Conference on Robotics and Automation (ICRA)*. IEEE, 2023, pp. 11 404–11 410.

[9] Q. Sun, W. Qi, H. Liu, X. Ji, and H. Qian, "Toward long-term sailing robots: State of the art from energy perspectives," *Frontiers in Robotics and AI*, vol. 8, p. 787253, 2022.

[10] L. Hertel and A. Schlaefer, "Data mining for optimal sail and rudder control of small robotic sailboats," in *Robotic Sailing 2012: Proceedings of the 5th International Robotic Sailing Conference*. Springer, 2013, pp. 37–48.

[11] F. Plumet, C. Petres, M.-A. Romero-Ramirez, B. Gas, and S.-H. Ieng, "Toward an autonomous sailing boat," *IEEE Journal of Oceanic Engineering*, vol. 40, no. 2, pp. 397–407, 2014.

[12] C. Sauzé and M. Neal, "A neuro-endocrine inspired approach to long term energy autonomy in sailing robots." 2010.

[13] Q. Sun, W. Qi, H. Liu, Z. Sun, T. L. Lam, and H. Qian, "Oceanvoy: A hybrid energy planning system for autonomous sailboat," in *2020 IEEE/RSJ International Conference on Intelligent Robots and Systems (IROS)*. IEEE, 2020, pp. 2481–2487.

[14] Q. Sun, W. Qi, X. Ji, and H. Qian, "V-stability based control for energy-saving towards long range sailing," *IEEE Robotics and Automation Letters*, vol. 8, no. 1, pp. 328–335, 2021.

[15] M. Wei and V. Isler, "Air to ground collaboration for energy-efficient path planning for ground robots," in *2019 IEEE/RSJ International Conference on Intelligent Robots and Systems (IROS)*. IEEE, 2019, pp. 1949–1954.

[16] C. Wu, C. Dai, X. Gong, Y.-J. Liu, J. Wang, X. D. Gu, and C. C. Wang, "Energy-efficient coverage path planning for general terrain surfaces," *IEEE Robotics and Automation Letters*, vol. 4, no. 3, pp. 2584–2591, 2019.

[17] S. Eiffert, N. D. Wallace, H. Kong, N. Pirmarzdashti, and S. Sukkarieh, "Resource and response aware path planning for long-term autonomy of ground robots in agriculture," *arXiv preprint arXiv:2105.10690*, 2021.

[18] L. Gan, J. W. Grizzle, R. M. Eustice, and M. Ghaffari, "Energy-based legged robots terrain traversability modeling via deep inverse reinforcement learning," *IEEE Robotics and Automation Letters*, vol. 7, no. 4, pp. 8807–8814, 2022.

[19] M. Adnane, B.-H. Nguyen, A. Khoumsi, and J. P. F. Trovão, "Driving mode predictor-based real-time energy management for dual-source electric vehicle," *IEEE Transactions on Transportation Electrification*, vol. 7, no. 3, pp. 1173–1185, 2021.

[20] S. F. Tie and C. W. Tan, "A review of energy sources and energy management system in electric vehicles," *Renewable and sustainable energy reviews*, vol. 20, pp. 82–102, 2013.

[21] N. Azim Mohseni, N. Bayati, and T. Ebel, "Energy management strategies of hybrid electric vehicles: A comparative review," *IET Smart Grid*, 2023.

[22] C. Di Franco and G. Buttazzo, "Coverage path planning for uavs photogrammetry with energy and resolution constraints," *Journal of Intelligent & Robotic Systems*, vol. 83, pp. 445–462, 2016.

[23] N. Bezzo, K. Mohta, C. Nowzari, I. Lee, V. Kumar, and G. Pappas, "Online planning for energy-efficient and disturbance-aware uav operations," in *2016 IEEE/RSJ International Conference on Intelligent Robots and Systems (IROS)*. IEEE, 2016, pp. 5027–5033.

[24] P. Tokekar, J. Vander Hook, D. Mulla, and V. Isler, "Sensor planning for a symbiotic uav and ugv system for precision agriculture," *IEEE transactions on robotics*, vol. 32, no. 6, pp. 1498–1511, 2016.

[25] R. Alyassi, M. Khonji, A. Karapetyan, S. C.-K. Chau, K. Elbassioni, and C.-M. Tseng, "Autonomous recharging and flight mission planning for battery-operated autonomous drones," *IEEE Transactions on*

Automation Science and Engineering, vol. 20, no. 2, pp. 1034–1046, 2022.

[26] S. G. Manyam, D. W. Casbeer, S. Darbha, I. E. Weintraub, and K. Kalyanam, "Path planning and energy management of hybrid air vehicles for urban air mobility," *IEEE Robotics and Automation Letters*, vol. 7, no. 4, pp. 10 176–10 183, 2022.

[27] Y. Bi, Y. Jin, H. Zhou, Y. Bai, C. Lyu, Z. Zeng, and L. Lian, "Surfing algorithm: Agile and safe transition strategy for hybrid aerial underwater vehicle in waves," *IEEE Transactions on Robotics*, 2023.

[28] M. N. Boukoberine, Z. Zhou, and M. Benbouzid, "A critical review on unmanned aerial vehicles power supply and energy management: Solutions, strategies, and prospects," *Applied Energy*, vol. 255, p. 113823, 2019.

[29] M. S. Rajabi, P. Beigi, and S. Aghakhani, "Drone delivery systems and energy management: A review and future trends," *arXiv preprint arXiv:2206.10765*, 2022.

[30] T. Lee, H. Kim, H. Chung, Y. Bang, and H. Myung, "Energy efficient path planning for a marine surface vehicle considering heading angle," *Ocean Engineering*, vol. 107, pp. 118–131, 2015.

[31] D. Kularatne, S. Bhattacharya, and M. A. Hsieh, "Time and energy optimal path planning in general flows." in *Robotics: Science and Systems*. Ann Arbor, MI, 2016, pp. 1–10.

[32] H. Niu, Z. Ji, A. Savvaris, and A. Tsourdos, "Energy efficient path planning for unmanned surface vehicle in spatially-temporally variant environment," *Ocean Engineering*, vol. 196, p. 106766, 2020.

[33] Y. Zhang, G. Shi, and J. Liu, "Dynamic energy-efficient path planning of unmanned surface vehicle under time-varying current and wind," *Journal of Marine Science and Engineering*, vol. 10, no. 6, p. 759, 2022.

[34] B. Li, B. R. Page, B. Moridian, and N. Mahmoudian, "Collaborative mission planning for long-term operation considering energy limitations," *IEEE Robotics and Automation Letters*, vol. 5, no. 3, pp. 4751–4758, 2020.

[35] A. Makhsoos, H. Mousazadeh, S. S. Mohtasebi, M. Abdollahzadeh, H. Jafarbiglu, E. Omrani, Y. Salmani, and A. Kiapey, "Design, simulation and experimental evaluation of energy system for an unmanned surface vehicle," *Energy*, vol. 148, pp. 362–372, 2018.

[36] L. Ma, X. Liu, Y. Zhang, and S. Jia, "Visual target detection for energy consumption optimization of unmanned surface vehicle," *Energy Reports*, vol. 8, pp. 363–369, 2022.

[37] X. Liang, P. Wang, X. Zhang, B. Wen, X. Li, and X. Tian, "Multi-objective robust energy management for environment powered unmanned surface vehicles," *Ocean Engineering*, vol. 247, p. 110624, 2022.

[38] F. Thompson, R. Galeazzi, and D. Guihen, "Field trials of an energy-aware mission planner implemented on an autonomous surface vehicle," *Journal of Field Robotics*, vol. 37, no. 6, pp. 1040–1062, 2020.

[39] C. A. Avizzano, P. Tripicchio, L. Joale, and M. Bergamasco, "Design of a motion based sailing simulator," in *19th International Symposium in Robot and Human Interactive Communication*. IEEE, 2010, pp. 1–7.

[40] F. Furrer and R. Siegwart, "Developing a simulation model of a catamaran using the concept of hydrofoils," *ETH Zurich*, 2010.

[41] M. Bühler, C. Heinz, and S. Kohaut, *Dynamic simulation model for an autonomous sailboat*. Universitäts-und Landesbibliothek Darmstadt, 2018.

[42] L. Xiao and J. Jouffroy, "Modeling and nonlinear heading control of sailing yachts," *IEEE Journal of Oceanic engineering*, vol. 39, no. 2, pp. 256–268, 2013.

[43] K. L. Wille, V. Hassani, and F. Sprenger, "Modeling and course control of sailboats," *IFAC-PapersOnLine*, vol. 49, no. 23, pp. 532–539, 2016.

[44] H. Abrougui and S. Nejim, "Backstepping control of an autonomous catamaran sailboat," *Robotic Sailing*, pp. 41–50, 2018.

[45] J. Melin, "Modeling, control and state-estimation for an autonomous sailboat," 2015.

[46] L. Jaulin and F. Le Bars, "Sailboat as a windmill," in *Robotic sailing 2013: proceedings of the 6th international robotic sailing conference*. Springer, 2013, pp. 81–92.

[47] H. Saoud, M.-D. Hua, F. Plumet, and F. Ben Amar, "Modeling and Control Design of a Robotic Sailboat," in *Robotic Sailing 2013*, F. L. Bars and L. Jaulin, Eds. Cham: Springer International Publishing, 2014, pp. 95–110.

[48] G. Elkaim and R. Kelbley, "Control architecture for segmented trajectory following of a wind-propelled autonomous catamaran," in *AIAA Guidance, Navigation, and Control Conference and Exhibit*, 2006, p. 6782.

[49] N. A. Cruz and J. C. Alves, "Auto-heading controller for an autonomous sailboat," in *OCEANS'10 IEEE SYDNEY*. IEEE, 2010, pp. 1–6.

[50] H. Saoud, M.-D. Hua, F. Plumet, and F. Ben Amar, "Modeling and control design of a robotic sailboat," in *Robotic Sailing 2013: Proceedings of the 6th International Robotic Sailing Conference*. Springer, 2014, pp. 95–110.

[51] T. I. Fossen, "Guidance and control of ocean vehicles," *University of Trondheim, Norway, Printed by John Wiley & Sons, Chichester, England, ISBN: 0 471 94113 1, Doctors Thesis*, 1999.

[52] T. I. Fossen, "Marine control systems–guidance. navigation, and control of ships, rigs and underwater vehicles," *Marine Cybernetics, Trondheim, Norway, Org. Number NO 985 195 005 MVA, www. marinecybernetics. com, ISBN: 82 92356 00 2*, 2002.

[53] H. Abrougui, S. Nejim, and H. Dallagi, "Modeling and autopilot design for an autonomous catamaran sailboat based on feedback linearization," in *2019 International Conference on Advanced Systems and Emergent Technologies (IC_ASET)*. IEEE, 2019, pp. 130–135.

[54] F. Zhang, X. Xiang, Y. Chen, S. Foong, and F. Maurelli, "Focused section on robotics and autonomy for sustainability," *International Journal of Intelligent Robotics and Applications*, pp. 1–3, 2023.

[55] Y. Dong, N. Wu, J. Qi, X. Chen, and C. Hua, "Predictive course control and guidance of autonomous unmanned sailboat based on efficient sampled gaussian process," *Journal of Marine Science and Engineering*, vol. 9, no. 12, p. 1420, 2021.

[56] T. I. Fossen, *Handbook of marine craft hydrodynamics and motion control*. John Wiley & Sons, 2011.

[57] Y. Emam, P. Glotfelter, S. Wilson, G. Notomista, and M. Egerstedt, "Data-driven robust barrier functions for safe, long-term operation," *IEEE transactions on robotics*, vol. 38, no. 3, pp. 1671–1685, 2021.

Qinbo Sun received the B.E. degree in Intelligence Science and Technology from Central South University (CSU), Changsha, China, in 2017, and the Ph.D. degree in Computer and Information Engineering of The Chinese University of Hong Kong, Shenzhen, China, in 2024, respectively.

He is currently a postdoc associate at Mohamed bin Zayed University of Artificial Intelligence (MBZUAI), and his research interests include field robotics, energy-aware robotic control, and egocentric environmental effects estimation.

Dr. Sun is a finalist for the IEEE/RSJ International Conference on Intelligent Robots and Systems (IROS) 2020 Best Application Paper Award.

Weimin Qi received her B.E. degree in Intelligence Science and Technology from Central South University (CSU), Changsha, China, in 2017, and the Ph.D. degree in Computer and Information Engineering of The Chinese University of Hong Kong, Shenzhen, China, in 2024, respectively.

She is currently a postdoc associate at Mohamed bin Zayed University of Artificial Intelligence (MBZUAI), and her research interests include field robotics, safety-critical navigation, and deployment in unstructured and dynamic environment.

Huihuan Qian (Member, IEEE) received the B.E. degree from the Department of Automation, University of Science and Technology of China, Hefei, China, in 2004, and the Ph.D. degree from the Department of Mechanical and Automation Engineering, The Chinese University of Hong Kong, Hong Kong, China, in 2010.

He is currently an Associate Professor with the School of Science and Engineering, The Chinese University of Hong Kong, Shenzhen, China, and the Associate Director of the Shenzhen Institute of Artificial Intelligence and Robotics for Society, Shenzhen. His research interests include robotics and intelligent systems, especially with a recent focus on marine robotics.